Tuning electrochemically-driven surface transformation in atomically-flat $LaNiO_3$ thin films for enhanced water electrolysis

Christoph Baeumer[1,2,3,‡✉], Jiang Li[4], Qiyang Lu[1,2,5,¶], Allen Yu-Lun Liang[2,6], Lei Jin[7], Henrique Perin Martins[5], Tomáš Duchoň[8], Maria Glöß[8,9], Sabrina M. Gericke[10,†], Marcus A. Wohlgemuth[8], Margret Giesen[8], Emily E. Penn[1,2], Regina Dittmann[8], Felix Gunkel[8], Rainer Waser[3,8], Michal Bajdich[4✉], Slavomír Nemšák[5,8✉], J. Tyler Mefford[1,2], William C. Chueh[1,2]

1 Department of Materials Science and Engineering, Stanford University, Stanford, CA 94305, USA
2 Stanford Institute for Materials and Energy Science, SLAC National Accelerator Laboratory, Menlo Park, CA 94025, USA
3 Institute of Electronic Materials (IWE2) and JARA-FIT, RWTH Aachen University, 52074 Aachen, Germany
4 SUNCAT Center for Interface Science and electrocatalysis, SLAC National Laboratory, Menlo Park, CA 94025, USA
5 Advanced Light Source, Lawrence Berkeley National Laboratory, Berkeley, California 94720, USA
6 Department of Chemistry, Stanford University, Stanford, CA 94305, USA
7 Ernst Ruska-Centre for Microscopy and Spectroscopy with Electrons (ER-C), Forschungszentrum Juelich GmbH, 52425 Juelich, Germany
8 Peter Gruenberg Institute and JARA-FIT, Forschungszentrum Juelich GmbH, 52425 Juelich, Germany
9 Leibniz-Institute of Surface Engineering (IOM), Permoserstraße 15, 04318 Leipzig, Germany
10 Chemical Science Division, Lawrence Berkeley National Laboratory, Berkeley, California 94720, USA
‡ Present address: MESA+ Institute for Nanotechnology, University of Twente, Faculty of Science and Technology, 7500 AE Enschede, Netherlands
¶ Present address: School of Engineering, Westlake University, Hangzhou, Zhejiang, 310024 China
† Present address: Combustion Physics, Lund University, Lund 22100, Sweden
✉ Corresponding authors: c.baeumer@utwente.nl; bajdich@slac.stanford.edu; SNemsak@lbl.gov

KEYWORDS: Electrolysis; Oxygen evolution reaction; Surface composition; Surface transformation, $LaNiO_3$; Standing wave photoemission, Metal-oxide coordination, Thermodynamics, Density Functional Theory

ABSTRACT

Structure-activity relationships built on descriptors of bulk and bulk-terminated surfaces are the basis for the rational design of electrocatalysts. However, electrochemically-driven surface transformations complicate the identification of such descriptors. Here, we demonstrate how the as-prepared surface composition of (001)-terminated $LaNiO_3$ epitaxial thin films dictates the surface transformation and the electrocatalytic activity for the oxygen evolution reaction. Specifically, the Ni termination (in the as-prepared state) is considerably more active than the La termination, lowering the overpotential by up to 150 mV. A combined electrochemical, spectroscopic and density-functional theory investigation suggests that this activity trend originates from a thermodynamically stable, disordered NiO_2 surface layer that forms during operation for Ni-terminated surfaces, which is kinetically inaccessible when starting with La-termination. Our work thus demonstrates tunability of surface transformation pathways by modifying a single atomic layer at the surface and that active surface phases only develop for select as-synthesized surface terminations.

INTRODUCTION

The need for sustainable, clean, and renewable energy has led to a resurging interest in water electrolysis[1] on perovskite-type oxides (ABO_3) because of the tunability of chemical and electrical properties through the choice of A- and B-site ions and substituents, and through controlling point defect concentrations.[2–5] Design improvements have resulted in earth-abundant electrocatalytic materials that outperform precious metal oxide benchmarks such as IrO_2 for the oxygen evolution reaction (OER) in alkaline electrolytes.[6–9] Approximate descriptors for OER activity trends such as electron occupancy of frontier orbitals,[8] electronic structure and relative orbital position,[10,11] and the density of oxygen vacancies[12] have been proposed.

While these OER descriptors are based on the bulk electronic structure of the perovskite, electrocatalytic activity is determined by the binding energies of reaction intermediates on the surface.[13] This reveals an inherent discrepancy because the bulk and the surface differ in composition as well as in electronic and geometric structures,[14,15] which has been repeatedly demonstrated for metallic systems.[6] The role of the perovskite oxide surface termination and reconstruction has been identified for a range of catalytic reactions occurring at elevated temperature at well-ordered solid/gas interfaces.[15–18] For electrochemical reactions at the solid/liquid interface, however, low-temperature surface transformation is typically accompanied by a loss of long-range order.[19] This makes quantification of the atomic surface arrangement through typical surface science techniques unattainable, particularly for oxide electrocatalysts.[20,21] Investigation of the surface composition of the transformed surface indicated a correlation between activity and surface composition.[22] But it has remained unclear how the surface properties of the as-synthesized perovskite oxides direct the surface transformation at the solid/liquid interface and, as a result, the OER activity. To address these issues, we need to derive the three-step relationship between (1) the as-prepared surface composition and phase, (2) the surface transformation pathway, and (3) the resulting electrocatalytic activity.

In this work, we derive the relationships between as-prepared surface composition, transformations, and activity in epitaxial $LaNiO_3$-based (LNO) electrocatalyst thin films, which are atomically flat both as-synthesized and during OER. Investigation of epitaxial perovskite thin films has revealed, e.g., the effects of subsurface and bulk stoichiometry,[23–25] substitution,[26,27] defect distributions and ordering,[28] and misfit strain.[29,30] Here, we go beyond these bulk-related properties and tune the as-prepared composition of the surface termination layer through sequential deposition and through film growth temperature. The surface and subsurface composition is depth-profiled with atomic-layer depth sensitivity using standing wave X-ray photoelectron spectroscopy (SW-XPS). We obtain information about the surface chemical environment from (typically bulk-sensitive) *operando* UV-Vis spectroelectrochemistry on films of various thicknesses ≤ 30 nm and spectral decomposition. We find that the as-prepared surface composition determines the surface transformation and, as a result, the OER activity. Specifically, the as-prepared Ni-termination undergoes a surface transformation and becomes active for OER, while preserving the surface cation stoichiometry of the as-prepared state. In contrast, La-termination leads to high overpotentials and does not transform to an active surface phase even after tens of hours of operation. Our experiments suggest the perovskite Ni-termination is transformed into a Ni oxyhydroxide-type single-layer surface phase. DFT reveals that such transformed surface layers are more active for OER due to the presence of triply coordinated O* reaction intermediates. We conclude that electrocatalytically active surface phases only develop for select as-synthesized surfaces, reflecting the crucial role of metastable surface transformations at room temperature. Our work showcases the tunability of surface transformation pathways through modifying a single atomic layer at the surface. It thus emphasizes the need for computational and experimental studies to develop structure-activity relationships involving surface-composition-dependent transformation pathways beyond established bulk and bulk-termination descriptors.

VARYING THE SURFACE TERMINATION IN EPITAXIAL $LaNiO_3$ LAYERS

To study the effect of surface composition and transformation on OER, one needs a model system of well-controlled bulk properties and an experimental lever to selectively change the composition of the surface layer. We selected $LaNiO_3$, a theoretically predicted[13] and experimentally demonstrated[12] high-activity OER electrocatalyst that avoids leaching of alkaline earth cation substituents.[31–33] To tune the surface composition, we used two independent approaches. First, we used sequential deposition of a single NiO_x layer on a La-terminated $LaNiO_3$ surface. Second, we varied the growth temperature during pulsed laser epitaxy of LNO thin films on (001)-oriented Nb:$SrTiO_3$ substrates. We found that this allows systematic variation of the surface termination. Tuning the surface composition through a high temperature treatment – a procedure generally employed in most oxide electrocatalyst fabrication pathways – makes the second approach relevant for a wide range of electrocatalysts.

For all films, the growth process proceeds in a two-dimensional manner, as demonstrated by *in situ* reflection high energy electron diffraction (Extended Data Fig. 1), resulting in step-terraced surface morphologies with low roughness. The bulk properties for 450 °C $\leq T^{\text{growth}} \leq$ 750 °C confirm high quality of the epitaxial growth and result in metallic thin films, as verified using X-ray diffraction, reciprocal space mapping, scanning transmission electron microscopy (STEM), inductively coupled plasma mass spectrometry (ICP-MS), and electrical transport characterization (Extended Data Fig. 1-2, Supplementary Notes 1-3 and Figs. 1-10).

To study the surface composition of the films grown at different temperatures, we turn to standing wave X-ray photoelectron spectroscopy, which is capable of depth-profiling the chemical environment in the near-surface region with 1-2 Å depth resolution.[34] Conventional analyses like laboratory and synchrotron XPS generally does not offer sufficient depth resolution and selectivity. We fabricated 20 nm LNO electrocatalyst layers at growth temperatures of 450°C and 650°C on X-ray mirrors consisting of 40 bilayers of four unit cells LNO and four unit cells $SrTiO_3$ (Figure 1a, Extended Data Fig. 3). These superlattices give rise to X-ray standing waves and depth-tunable

photoexcitation probability (Supplementary Notes 4,5 and Extended Data Fig. 3). Analysis of the SW-XPS data is based on spectral deconvolution of the Ni 3*p* and La 4*d* core levels, where La 4*d* exhibits surface and bulk components (Extended Data Fig. 4). Figs. 1b,c show the so-called rocking curves (core-level intensity evolutions as a function of incidence angle) for both samples in the as-prepared state (see Supplementary Fig. 11 for the rocking curves of all detectable photoelectron spectra). We find that the rocking curves for Ni 3*p* and La 4*d*(surface) are in phase for the T^{growth} = 450 °C film, whereas they are out of phase for the T^{growth}=650 °C film. For the latter, Ni 3*p* and La 4*d*(bulk) are in phase, qualitatively indicating that the surface is Ni-rich when grown at 450 °C and La-rich when grown at 650 °C, in agreement with laboratory XPS analysis for samples without underlying X-ray mirror (Extended Data Fig. 4). Using the SWOPT optimizer for a quantitative SW-XPS analysis[35] (a structure model optimization process iteratively comparing experimental to calculated XPS rocking curves, see Methods and Supplementary Note 5), we fit a composition profile to these rocking curves using combined X-ray optical and photoemission calculations.

The best fit was obtained with a Ni-free surface layer of 3 Å thickness for the T^{growth} = 650 °C film and a 3 Å-thick Ni-rich surface for the T^{growth} = 450 °C film (Fig. 1d-f). STEM investigation with atomic resolution energy-dispersive X-ray spectroscopy (EDX) confirms that for T^{growth} = 650 °C, the surface exhibits a mixture of LaO termination and a double LaO_x layer on the surface (Fig. 1f,g), which corresponds well to the 3 Å Ni-free layer observed in SW-XPS. We thus assign predominant Ni termination (LNO-Ni) to the films grown at low temperature (450 - 550 °C) and mixed single and double La termination layers (LNO-La and LaO_2|LNO-La) to films grown at intermediate temperatures (650 °C). For T^{growth} = 750 °C, the Ni-free surface layer is even thicker, as shown by laboratory XPS results (Extended Data Fig. 4). Thus, tuning the temperature during deposition gives us selective control of surface composition while keeping the bulk stoichiometry constant and the morphology comparably smooth. This change of surface termination is related to differences in thermodynamic stability (Supplementary Notes 1-3).

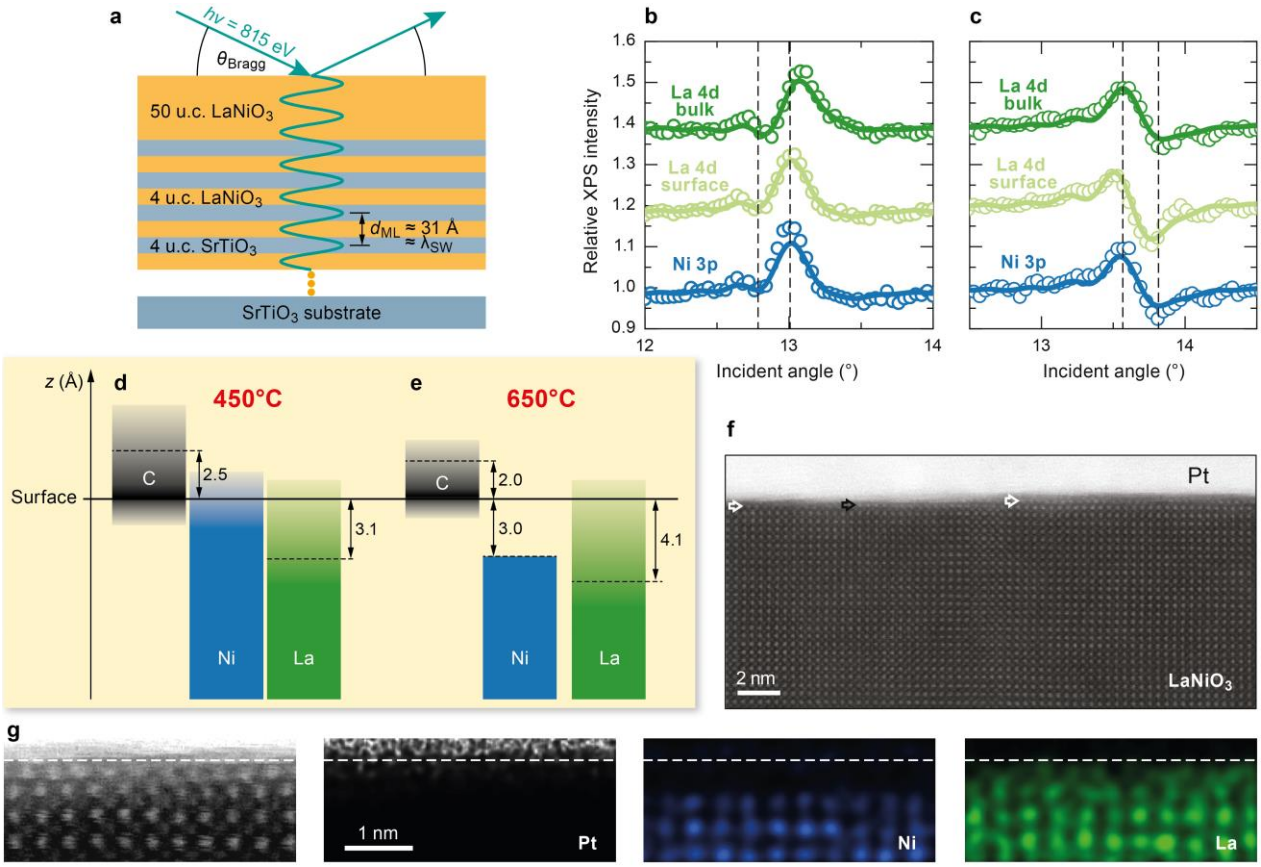

Figure 1: Standing wave XPS analysis. a, Schematic of the investigated multilayer capped by a 50 u.c. LNO electrocatalyst layer. The vertical position of antinodes of the X-ray standing waves can be shifted by varying the incident angle, resulting in precise depth-selective photoemission intensity modulations. **b,** and **c,** La 4*d* and Ni 3*p* SW-XPS rocking curves for LNO top layers deposited at 450 and 650°C, respectively. Open circle data points and solid lines represent measured intensities and best fitting results, respectively. The dotted lines are guides to the eye to illustrate phase shifts between La and Ni. **d,** and **e,** Optimized models used to simulate the rocking curves in b and c, respectively. Light green indicates La surface species, dark green indicates La bulk species. Adventitious carbon was used for calibration of the fitting routine. **f,** STEM dark field image for $T^{growth} = 650°C$. White (black) arrows indicate LaO_x on LaO (LaO-only) terminating layers. **g,** High-resolution STEM dark field image and EDX distribution of Pt, Ni and La for the same sample as in panel f. The dotted line indicates the interface between the LNO and a protective Pt capping layer. Double LaO terminating layers are visible in this region. Note that direct TEM imaging of the suspected Ni termination for $T^{growth} = 450°C$ and $T^{growth} = 550°C$ was challenging because of weaker contrast and a higher density of defects (see Supplementary Note 1). We therefore rely on spectroscopic analysis for these films and consider the TEM investigation shown here as a validation of the SW-XPS analysis.

SURFACE COMPOSITION VARIATIONS DICTATE OER ACTIVITY

We explored the role of the as-prepared surface composition for the OER using our LNO films of 20 nm thickness (Figure 2, Supplementary Note 6 and Extended Data Fig. 5). The films remain atomically smooth during cyclic voltammetry (CV, Fig. 2a-c and Extended Data Figs. 1, 6). We first observe a striking difference in the pre-OER regime during cyclic voltammetry: LNO-

Ni features a characteristic redox wave at a potential of ~1.4 V vs. RHE (Fig. 2d). This redox wave is absent for La-covered surfaces (Fig. 2d) and remains negligible even after tens of CV cycles or 16 hours of chronoamperometry at various potentials (Extended Data Fig. 7h). The magnitude of the redox wave decreases monotonically with increasing La coverage, and for LNO-Ni it corresponds to the charge expected for an oxidation/reduction of approximately one layer of Ni ions (Fig. 2e), in line with a sweep-rate dependence that suggests a surface-limited redox process (Extended Data Fig. 7).

All LNO films exhibited considerable OER activities, ranging from overpotential η of 0.5 V to 0.6 V at a current density of 1 mA cm^{-2}, normalized to the real, geometric surface area (Fig. 2b). The Ni-termination (LNO-Ni) achieved through low growth temperatures or sequential deposition exhibits the highest activity, followed by mixed LNO-La and LaO_x|LNO-La, and thicker La-type surface layers. This activity difference does not correlate with the observed differences in the bulk properties: all films have identical bulk composition exhibit a high electrical conductivity (Extended Data Fig. 2 and Supplementary Fig. 4). The transport properties do vary with temperature, but the highest electrical conductivity is observed for rather inactive samples (T^{growth} = 650 °C). The lowest conductivity is found for T^{growth} = 450 °C, but nonetheless the OER activity is higher than for T^{growth} = 650 °C. Consistently, cyclic voltammetry in the presence of the outer sphere fast redox couples $[Fe(CN)_6]^{3-/4-}$ and $[Ru(NH_3)_6]^{2+/3+}$ demonstrates closely spaced, symmetric redox peaks, confirming electrical conductivity does not limit the performance of the different electrodes (Supplementary Fig. 12). We therefore surmise that the activity differences are a direct result of the as-prepared surface composition, as confirmed through similar activities across a wide potential range for LNO-Ni achieved through low deposition temperatures and through sequential deposition, respectively. This is expectable but rarely demonstrated for electrocatalysts, where surface adsorption energetics and electron transfer properties of reaction intermediates are determined by the chemical identity of the surface active sites. Interestingly, our LNO-Ni also exhibits the highest activity amongst LNO thin films reported in the literature

(Extended Data Fig. 8 and Supplementary Tables 1 and 2), which points to the origins of electrocatalytic activity differences amongst nominally identical bulk compositions. Finally, the LNO-Ni films exhibited good stability, with stable OER at 1 mA cm^{-2} for at least 40 hours (Fig. 2f). The LNO-La films, on the other hand, exhibited catastrophic failure after 7-10 h, likely due to additional decomposition reactions occurring at the high overpotentials required for the chosen current density (η > 0.5 V).

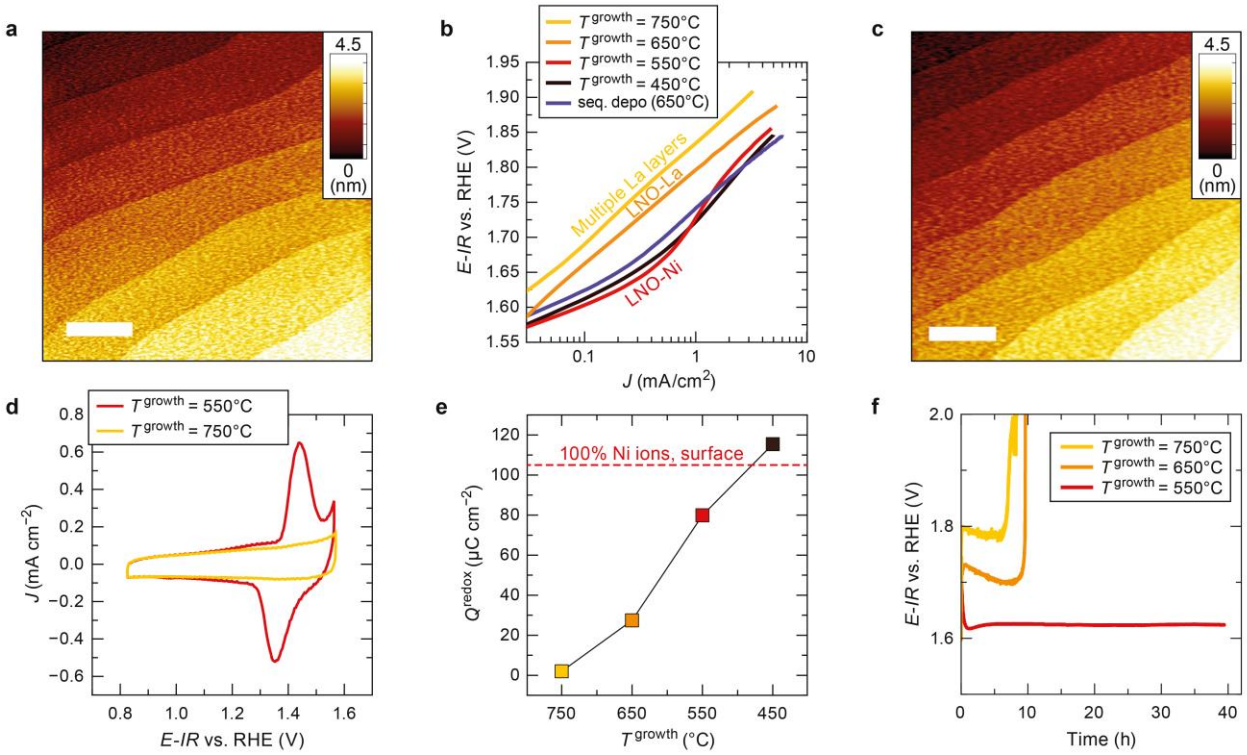

Figure 2: Electrochemical performance. a, Atomic force micrograph of the as-prepared state of a 20 nm $LaNiO_3$ film with T^{growth} = 550 °C obtained using ultra-high vacuum transfer from the growth to the characterization chamber. Scale bar is 1 µm, step height is ~0.4 nm. **b,** OER activity for different surface compositions in a Tafel-like plot. Ni-termination was achieved through low-T growth or deposition of a single NiO_x layer on LNO-La. **c,** Atomic force micrograph of the same sample as in **a** after cyclic voltammetry with 52 cycles (maximum potential ~1.6 V vs. RHE) and 2 cycles with maximum potential of ~1.9 V vs. RHE. **d,** Cyclic voltammetry at 500 mV/s in the Ni^{2+} – Ni^{3+} redox area for samples with low and high growth temperature. **e,** Redox charge of the Ni^{2+} – Ni^{3+} conversion during cyclic voltammetry. Line is a guide to the eye and indicates the expected charge for a pure surface process involving 100 % of the Ni ions in LNO-Ni. The absence of a thickness dependence indicates a surface-related process. **f,** Chronopotentiometry at a current density of 1 mA/cm^2. The T^{growth} = 550 °C sample did not degrade in the time tested here, the samples fabricated at higher T^{growth} underwent catastrophic failure after 7.5 or 10.3 h (sharp increase in potential).

SPECTROSCOPIC INSIGHT INTO THE ROLE OF SURFACE TRANSFORMATIONS

We now explore surface transformations of LNO-Ni and LNO-La, motivated by the previous suggestions of transformation of perovskite-oxide surfaces and the formation of (oxy-)hydroxide-like layers.[36] First, we consider possible surface reconstructions that also typically occur for well-ordered surfaces at the solid/gas interface at elevated temperatures. Low energy electron diffraction before and after OER without exposure to air, following the approach suggested by Faisal et al.[20] reveals that after cyclic voltammetry, the original perovskite diffraction pattern disappears (Supplementary Fig. 13), suggesting a loss of long range order during the electrochemically-induced surface transformation although the surface morphology remained atomically flat and unit-cell-height step-terraced.

Because it is challenging to structurally characterize surface transformations that occur at room temperature, we developed an approach using *operando* ultraviolet–visible absorption (UV-Vis) spectroelectrochemistry applied to thickness-controlled films to differentiate between surface and bulk redox processes and to identify the chemical nature of this disordered surface layer. As shown in Figure 3a-d, an optical density (*OD*) change occurs at a potential of ~1.4 V vs. RHE for LNO-Ni, which is absent in LNO-La. Comparison to reference measurements reveals that this characteristic spectral change at around λ = 500 nm is similar to the spectral change in hexagonal NiO_xH_y (Supplementary Note 7 and Extended Data Fig. 9). In LNO-Ni as well as in NiO_xH_y, the characteristic spectral change coincides with the observed redox wave at a potential of ~1.4 V vs. RHE in cyclic voltammetry in the pre-OER region (Fig. 3c-d and Extended Data Fig. 9).

Next, we make use of our epitaxial thin film approach to deconvolute spectral changes from the LNO bulk and from the surface layer through the comparison of samples with various precisely-controlled thicknesses. The redox feature in cyclic voltammetry as well as the optical density change at 1.4 V vs. RHE do not depend on the sample thickness (Fig. 3f and Supplementary Fig. 14). Correspondingly, spectral deconvolution into a bulk-related contribution (occurring across the entire potential range) and a surface-related contribution (occurring mostly near the redox

potential) shows that the optical density change related to the Ni oxidation stems from the top 1-2 unit cells (Supplementary Note 7).

We distinguish surface- and bulk related properties using the differential optical density variation at $\lambda = 500$ nm (characteristic for hexagonal NiO_xH_y) and $\lambda = 700$ nm (characteristic for bulk LNO). For LNO-Ni, we find a surface related optical density jump at the redox potential, which does not occur for LNO-La (Fig. 3e). These observations imply that the electrocatalytically-active transformation occurring for LNO-Ni (which is absent for LNO-La) likely corresponds to a Ni oxyhydroxide-type surface layer, in reasonable agreement with recent observations of local amorphization of up to two LNO layers (with unspecified surface composition) at the onset of OER.[37] The role of this surface phase transformation will be explored computationally below. Importantly, we emphasize again that this transformation to an electrocatalytically-active surface occurs only for LNO-Ni, and not for LNO-La. For additional validations of the surface phase transformation, we compared LNO-Ni and LNO-La surfaces before and after OER using lab-based XPS, SW-XPS, and cluster-model spectral simulations. For LNO-Ni, we find a 4 Å surface layer, consistent with a Ni oxyhydroxide signature (Supplementary Fig. 15 and Supplementary Note 8).

Our observation that the electrocatalytically-active surface phase only forms for LNO-Ni may also explain the doubling of OER current density (at 1.63 V vs. RHE) compared to the most active LNO thin films reported in the literature (Extended Data Fig. 8 and Supplementary Tables 1 and 2). These films likely exhibited La termination, which is thermodynamically favorable at high growth temperatures. Our results, in contrast, show that optimal activities can be achieved by tuning the surface composition of the as-prepared state. Importantly, the activity trends observed here are generalizable for LNO fabricated in different morphologies and shapes, as previous reports for particulate LNO electrocatalysts found low calcination temperatures to lead to optimal performance for CO oxidation,[38] oxygen evolution,[39] and oxygen reduction reactions (accounting for variations in surface area).[40]

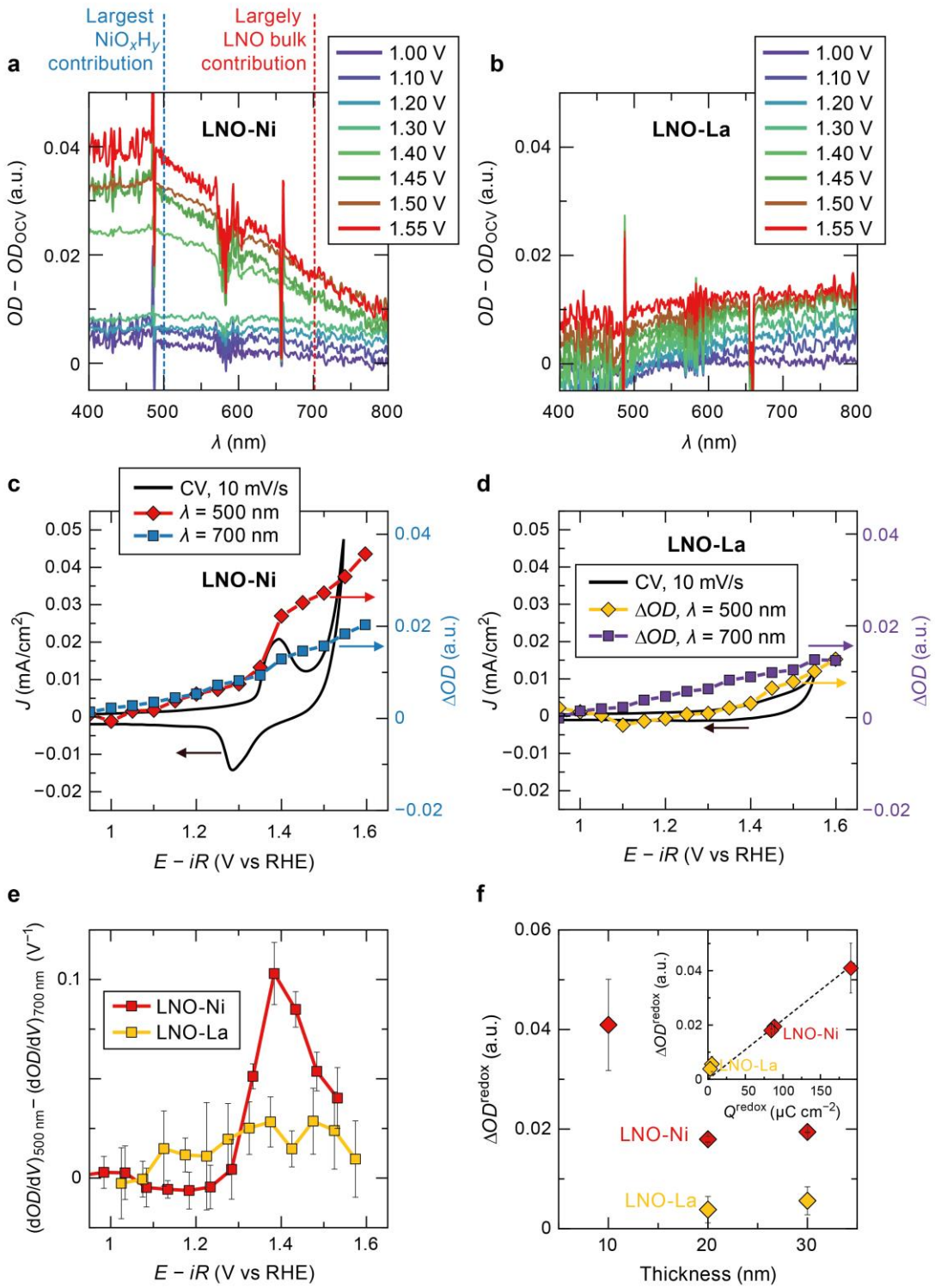

Figure 3: ***Operando*** **UV-Vis spectroelectrochemistry of $LaNiO_3$. a, b,** Optical density changes in LNO-Ni and LNO-La as a function of applied potential. **c,. d,** Cyclic voltammetry at 10 mV/s in the pre-OER region LNO-Ni and LNO-La, respectively, along optical density change at λ = 500 nm and λ = 700 nm during potential holds **e,** Difference in differential optical density variation at λ = 500 nm and λ = 700 nm for LNO-Ni and LNO-La. The peak near 1.4 V vs. RHE only occurs for LNO-Ni and confirms a surface-related process. **f** Optical density change at λ = 500 nm as a function of LNO thickness. Inset: Optical density change as a function of redox charge of the Ni^{2+} – Ni^{3+} conversion during cyclic voltammetry. Line is a linear fit.

ATOMISTIC INSIGHTS INTO THE ROLE OF SURFACE TERMINATION FOR OER

Based on the experimental realization of LNO with different surface terminations in the as-prepared state and a termination-dependent surface phase transformation, we now turn to the theoretical investigation of the OER activity using computed thermodynamics. For completeness, we first investigate LNO-Ni and LNO-La (001) perovskite-type terminations for OER. We start from the optimized tetragonal, metallic, and paramagnetic LNO bulk phase as calculated via DFT with Hubbard-*U* matching experimental crystallographic and electronic properties (see Methods and Supplementary Fig. 16). Figure 4a shows the surface Pourbaix diagram of bulk terminated LNO-Ni.[41,42] As the voltage increases, the LNO-Ni surface progresses from more reduced to more oxidized coverages (V_O < H < OH < O). Notably, the presence of oxygen vacancies (V_O) on the LNO-Ni surface is limited to voltages below 0.45 V vs. RHE, while subsurface V_O are energetically less favorable (+0.9 eV, Supplementary Fig. 17). While VO may exist and differ in concentration among the as-deposited films, they are likely eliminated under OER conditions given the high effective p_{O2} of ~10^{70} atm at 1.68 V vs. RHE At the relevant OER potentials, the surface is preferably covered by a monolayer of H* on singly coordinated O_{1c} ("OH_{top}") and a half monolayer of H* on doubly coordinated O_{2c} ("H_{bridge}") (LNO-Ni-S_4 coverage in Fig. 4). This coverage was also identified by Rong *et al.*.[43] Also noticeable is the high voltage (> 2 V) required to reach one monolayer of O^*_{top} (LNO-Ni-S_6). The LNO-La surface prefers adsorption in the La-O-La bridge configuration (O_{2c}), but otherwise, the situation is similar to LNO-Ni (Extended Data Fig. 10a). One monolayer OH^*_{bridge} coverage (LNO-La-S_4) is dominant under OER conditions, and high voltage (> 2 V) is needed to reach any O* intermediate.

Using the surface Pourbaix diagrams results, we evaluate the OER theoretical activity of LNO, as shown in Fig. 4b. Calculating the theoretical overpotential self-consistently, i.e., considering only the stable S_4 coverages for LNO-Ni and LNO-La, we find that for both surfaces the potential limiting step is from OH* → O* (step 2 of OER single site mechanism, Fig. 4b). For O_{1c} (O_{2c}) on LNO-Ni, the thermodynamic OER overpotential is η=1.13 V (η=0.90 V). On LNO-La, there is

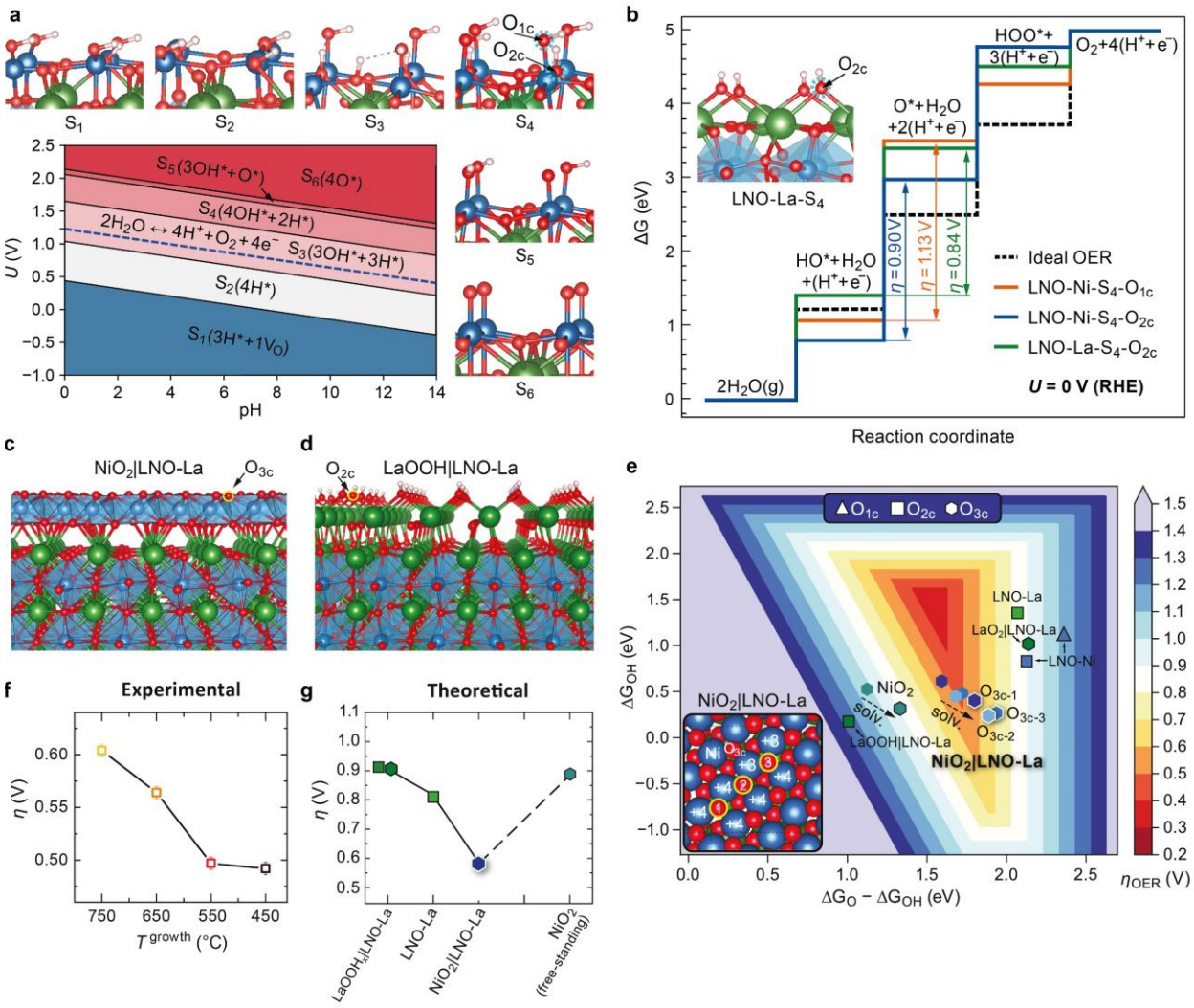

Figure 4: **OER overpotentials for LNO surfaces and oxide|LNO interfaces. a,** Surface Pourbaix diagram of LNO-Ni Additional surface Pourbaix diagrams are shown in Extended Data Fig. 10. Labels from Ni-S_1 to Ni-S_5 designate surface coverages from more reduced to more oxidized, with corresponding (2×2) structures as insets. The thermodynamic H_2O vs. O_2 equilibrium is indicated by blue dashed line. Under OER conditions (U_{RHE}~1.68 V), the most stable LNO-Ni surface is covered with 1 monolayer OH_{top}* on top of Ni sites and 0.5 monolayers H^*_{bridge} (LNO-Ni-S_4). **b,** Calculated OER free energy diagram for LNO-Ni-S_4 at the top-site (orange) and at the bridge-site (blue) and for LNO-La-S_4 at the bridge-site (green, compare inset) are compared to an ideal electrocatalyst (dashed line) at no bias (all four charge transfer steps having identical reaction free energies of 1.23 eV). **c,d,** Structural models of the most stable interfaces for NiO_2|LNO-La and LaOOH|LNO-La. **e,** OER activity volcano shown as a 2D heat-map of overpotentials based on mapping to OH*, O*, and scaled OOH* values placing individual structures according to their descriptor value. The inset shows the top view of NiO_2|LNO-La, which highlights three types of hollow oxygen sites O_{3c} with mixed Ni^{4+}/Ni^{3+} valence of the overlayer (hexagons in the volcano plot). The activity of O_{3c} sites in the free standing NiO_2(hex) layer is also shown (teal hexagons). Solvation corrections for all NiO_2(hex) surfaces are shown as white-edge hexagons. **f,** Comparison of the experimental overpotential for a current density of 1 mA cm^{-2}. **g,** Theoretical overpotentials for selected terminations matching the trend from experiment qualitatively. See Supplementary Table 5 for a list of all calculated overpotentials.

only O_{2c} with η=0.84 V. While LNO-La is found to be slightly more active than LNO-Ni, both perovskite-type LaO and NiO bulk terminations of LNO (001) have unfavorable O* intermediates which force the metal sites to be in unfavorable Ni^{4+} and $La^{3.5+}$ oxidation states during these intermediate steps, resulting in high overpotentials. These are in stark relative and quantitative disagreement with experiment (η of 0.50 V and 0.58 V for LNO-Ni and LNO-La, respectively, at a current density of 1 mA cm^{-2}). Using the perovskite-type terminations, such low overpotentials can only be predicted by invoking alternative reaction mechanisms away from the DFT self-consistent coverage (such as adding V_O or removing H_{bridge}, Supplementary Fig. 18)[43] or through unphysically large Hubbard-U values for Ni (U>6 eV) in metallic LNO.[44] In short, bulk terminations of LNO (001) with realistic coverages under OER conditions have a strong preference towards high coverage of OH* and require large overpotentials to turn over to O*.

We now turn to the transformed, electrocatalytically-active, disordered Ni oxyhydroxide-type layer surface. Computational OER studies of layered oxides, oxy-hydroxides, and related studies of their overlayers[45–49] are all based on hexagonal, edge-sharing octahedra and layered-type structures, which are very distinct from corner-sharing octahedra found in LNO. Therefore, we consider transformations of the bulk-terminated LNO-Ni using layered, edge-sharing NiO_2-type building blocks as a likely approximation of the local order within the disordered Ni oxyhydroxide-type surface layer. For LNO-La, we consider additional overlayers with LaO_2H_x and La_2O_3 building blocks, motivated by the observed multiple La-layers for high T^{growth} (compare Fig. 1). Utilizing the MPInterfaces code,[50] we have selected and optimized structures with minimal lattice strain, which we expect to reflect the most likely local binding environments. The results summarized in Fig. 4 and Supplementary Figs. 19 and 20 show that for LNO-Ni, a 4×4 NiO_2(hex) transformation on (2×2)LNO-La is very stable (labeled as NiO_2|LNO-La in Fig. 4c), since it maximizes the available oxygen bonding to LNO-La with minimal distortion of the overlayer. This hexagonal NiO_2 layer can be interpreted as the short-range-ordered, fully oxidized form of the Ni hydroxide suggested by the experimental redox properties and UV-Vis spectroelectrochemistry.

Importantly, the oxidative removal of H* from this reconstructed surface occurs at potentials of ~1.45 V vs. RHE (as shown in the surface Pourbaix diagram in Extended Data Fig. 10b). This value matches the experimentally observed redox peaks much better than the corresponding DFT-predicted potential of >2 V vs. RHE for LNO-Ni or LNO-La bulk terminations, suggesting that such a NiO_2|LNO-La configuration is a good approximation of the experimentally observed transformed surface. For terminations consisting of La-double layers, a (2×2) LaO+OH layer on (2×2) LNO-La forms the most stable structure at OER conditions (LaOOH|LNO-La in Fig. 4d). Under more oxidizing potentials, this structure can transform to a more oxidized LaO_2|LNO-La type overlayer. Less stable combinations of overlayers are summarized in Supplementary Fig. 20. Considering the most stable overlayers for Ni (NiO_2|LNO-La, Fig. 4c) and for La (LaOOH|LNO-La, Fig. 4d, and LaO_2|LNO-La) as reasonable representations of the most likely local surface structures under applied potential, we calculate the theoretical OER overpotential.

Fig. 4e shows the results for theoretical OER activities as a 2D heat-map volcano of OER overpotentials. For bulk terminations of LNO (001) under OER, both LNO-Ni-S_4 and LNO-La-S_4 feature a weakly adsorbed O* either as O_{1c} or O_{2c}, as discussed above, and are located on the right side of the 2D map. LaOOH|LNO-La or LaO_2|LNO-La, which are likely present for the samples with high T^{growth}, feature much less active oxygen sites with even higher overpotentials than for LNO-La bulk termination (η = 0.92 and 0.91 V, respectively).

When we consider the NiO_2|LNO-La transformation of the as-prepared LNO-Ni surface, the thermodynamic overpotentials are lowered dramatically. The basal plane of the layered NiO_2 overlayers features triple-coordinated O_{3c} sites with mixed Ni^{4+}/Ni^{3+} valence (inset of Fig. 4e). The triple bonding leads to significant stabilization of O* and OH*, and results in an overall shift to a lower and more centered position on the 2D volcano map. The calculated overpotentials are η=0.49 V, 0.54 V, and 0.61 V for the three distinguishable O_{3c} lattice sites. After adding solvation effects, the results for NiO_2|LNO-La are slightly modified, leading to stabilized OH* (η=0.7 V, 0.57 V, and 0.65 V, white-edged hexagons in Fig. 4c, see Supplementary Fig. 21 for

solvation models). Combined with our experimental spectroelectrochemistry results and previous observations from X-ray spectroscopy,[36] the agreement of the computational thermodynamic overpotential with the experimental overpotential for LNO-Ni suggests that transformed Ni oxyhydroxide-like surfaces dominate the electrocatalytic activity. Our DFT calculations also show that this NiO_2|LNO-La surface is thermodynamically more stable under OER conditions than all other surfaces considered here (Supplementary Figs. 19-20), rendering this spectroscopically-suggested surface transformation pathway plausible. However, this surface transformation is kinetically accessible only when starting with a Ni perovskite termination. The La terminations are not converted to Ni oxyhydroxide-like surfaces throughout their lifetime of several hours. To assess the effect of the NiO_2|LNO buried interface, we also evaluated the theoretical overpotential for freestanding, single-layer NiO_2, which only features Ni^{4+}. We obtain a considerably larger overpotential of 0.89 V, indicating the important role of the underlying perovskite lattice, in agreement with the experimental test of single layer of NiO_x on different support layers (Supplementary Fig. 22).

CONCLUSION

We investigated atomically flat, (001) Ni- and La- terminated LNO films. We find experimentally that the surface termination is decisive for the transformation pathway and the resulting electrocatalytic activity. The as-prepared surface can be tuned through both the growth temperature and through sequential deposition. Through the surface-sensitive information from UV-Vis spectroelectrochemistry applied to thin films, we find that thermodynamically stable Ni hydroxide-like surface transformations (~one atomic layer) develop on Ni-terminated perovskite surfaces, lowering the OER overpotential by up to 150 mV compared to La-based surface terminations, in agreement with DFT-predicted thermodynamic overpotentials. This electrochemically-driven transformation is inaccessible when starting from La-termination. Therefore, the electrocatalytic activity of perovskite oxides cannot be predicted without considering such transformations. Our combined theoretical and experimental investigation

suggests that the underlying bulk perovskite structure still plays an important role in activation of the overlayers. Identification and prediction of future high-activity electrocatalysts should therefore consider the three-step relationship observed here as an addition to bulk-related descriptors: (1) the as-prepared surface composition determines (2) the surface transformation pathway which in turn governs (3) the electrocatalytic activity. Further development of local-structure-sensitive *operando* probes of the electrocatalyst surface layer are needed for unequivocal identification of such transformations. Technologically tuning the surface composition a priori to unlock a particularly active transformation pathway offers an attractive additional avenue for future electrocatalyst research and exploitation.

REFERENCES

1. Fabbri, E., Habereder, A., Waltar, K., Kötz, R. & Schmidt, T. J. Developments and perspectives of oxide-based catalysts for the oxygen evolution reaction. *Catal. Sci. Technol.* **4**, 3800–3821 (2014).
2. Kubicek, M., Bork, A. H. & Rupp, J. L. M. Perovskite oxides – a review on a versatile material class for solar-to-fuel conversion processes. *J. Mater. Chem. A* **5**, 11983–12000 (2017).
3. Hwang, J. *et al.* Perovskites in catalysis and electrocatalysis. *Science* **358**, 751–756 (2017).
4. Antipin, D. & Risch, M. Trends of epitaxial perovskite oxide films catalyzing the oxygen evolution reaction in alkaline media. *J. Phys. Energy* **2**, 032003 (2020).
5. Bick, D. S. *et al.* Stability and Degradation of Perovskite Electrocatalysts for Oxygen Evolution Reaction. *Electrochim. Acta* **218**, 156–162 (2016).
6. Seh, Z. W. *et al.* Combining theory and experiment in electrocatalysis: Insights into materials design. *Science* **355**, eaad4998 (2017).
7. Hong, W. T. *et al.* Charge-transfer-energy-dependent oxygen evolution reaction mechanisms for perovskite oxides. *Energy Environ. Sci.* **10**, 2190–2200 (2017).
8. Suntivich, J., May, K. J., Gasteiger, H. A., Goodenough, J. B. & Shao-Horn, Y. A Perovskite Oxide Optimized for Oxygen Evolution Catalysis from Molecular Orbital Principles. *Science* **334**, 1383–1385 (2011).
9. Montoya, J. H. *et al.* Materials for solar fuels and chemicals. *Nat. Mater.* **16**, 70–81 (2017).
10. Yamada, I. *et al.* Systematic Study of Descriptors for Oxygen Evolution Reaction Catalysis in Perovskite Oxides. *J. Phys. Chem. C* **122**, 27885–27892 (2018).
11. Grimaud, A. *et al.* Activating lattice oxygen redox reactions in metal oxides to catalyse oxygen evolution. *Nat. Chem.* **9**, 457–465 (2017).
12. Mefford, J. T. *et al.* Water electrolysis on $La_{1-x}SrxCoO3-\delta$ perovskite electrocatalysts. *Nat. Commun.* **7**, 11053 (2016).
13. Man, I. C. *et al.* Universality in Oxygen Evolution Electrocatalysis on Oxide Surfaces. *ChemCatChem* **3**, 1159–1165 (2011).
14. Lee, Y.-L., Kleis, J., Rossmeisl, J. & Morgan, D. Ab initio energetics of LaBO3 (001) (B = Mn , Fe, Co, and Ni) for solid oxide fuel cell cathodes. *Phys. Rev. B* **80**, 224101 (2009).
15. Riva, M. *et al.* Influence of surface atomic structure demonstrated on oxygen incorporation mechanism at a model perovskite oxide. *Nat. Commun.* **9**, 3710 (2018).
16. Stoerzinger, K. A. *et al.* Influence of LaFeO3 Surface Termination on Water Reactivity. *J. Phys. Chem. Lett.* **8**, 1038–1043 (2017).
17. Huang, K. *et al.* Engineering the surface of perovskite La0.5Sr0.5MnO3 for catalytic activity of CO oxidation. *Chem. Commun.* **50**, 9200–9203 (2014).
18. Polo-Garzon, F. *et al.* Understanding the Impact of Surface Reconstruction of Perovskite Catalysts on CH4 Activation and Combustion. *ACS Catal.* **8**, 10306–10315 (2018).
19. Chung, D. Y. *et al.* Dynamic stability of active sites in hydr(oxy)oxides for the oxygen evolution reaction. *Nat. Energy* **5**, 222–230 (2020).
20. Faisal, F. *et al.* Electrifying model catalysts for understanding electrocatalytic reactions in liquid electrolytes. *Nat. Mater.* **17**, 592–598 (2018).
21. Rao, R. R. *et al.* Towards identifying the active sites on RuO2 (110) in catalyzing oxygen evolution. *Energy Environ. Sci.* **10**, 2626–2637 (2017).
22. Scholz, J. *et al.* Tailoring the Oxygen Evolution Activity and Stability Using Defect Chemistry. *Catalysts* **7**, 139 (2017).

23. Wang, L. *et al.* Tuning Bifunctional Oxygen Electrocatalysts by Changing the A-Site Rare-Earth Element in Perovskite Nickelates. *Adv. Funct. Mater.* **28**, 1803712 (2018).
24. Bak, J., Bae, H. Bin, Kim, J., Oh, J. & Chung, S.-Y. Formation of Two-Dimensional Homologous Faults and Oxygen Electrocatalytic Activities in a Perovskite Nickelate. *Nano Lett.* **17**, 3126–3132 (2017).
25. Eom, C. J. *et al.* Tailoring manganese oxide with atomic precision to increase surface site availability for oxygen reduction catalysis. *Nat. Commun.* **9**, 4034 (2018).
26. Bak, J., Bin Bae, H. & Chung, S. Y. Atomic-scale perturbation of oxygen octahedra via surface ion exchange in perovskite nickelates boosts water oxidation. *Nat. Commun.* **10**, 2713 (2019).
27. Liu, J. *et al.* Tuning the Electronic Structure of LaNiO3 through Alloying with Strontium to Enhance Oxygen Evolution Activity. *Adv. Sci.* **1901073**, 1901073 (2019).
28. Gunkel, F. *et al.* Ordering and phase control in epitaxial double-perovskite catalysts for the oxygen evolution reaction. *ACS Catal.* **7**, 7029–7037 (2017).
29. Wang, L. *et al.* Strain Effect on Oxygen Evolution Reaction Activity of Epitaxial NdNiO3 Thin Films. *ACS Appl. Mater. Interfaces* **11**, 12941–12947 (2019).
30. Liu, X. *et al.* Uncovering the Effect of Lattice Strain and Oxygen Deficiency on Electrocatalytic Activity of Perovskite Cobaltite Thin Films. *Adv. Sci.* **6**, 1801898 (2019).
31. Risch, M. *et al.* La 0.8 Sr 0.2 MnO 3−δ Decorated with Ba 0.5 Sr 0.5 Co 0.8 Fe 0.2 O 3−δ : A Bifunctional Surface for Oxygen Electrocatalysis with Enhanced Stability and Activity. *J. Am. Chem. Soc.* **136**, 5229–5232 (2014).
32. Geiger, S. *et al.* The stability number as a metric for electrocatalyst stability benchmarking. *Nat. Catal.* **1**, 508–515 (2018).
33. May, K. J. *et al.* Influence of Oxygen Evolution during Water Oxidation on the Surface of Perovskite Oxide Catalysts. *J. Phys. Chem. Lett.* **3**, 3264–3270 (2012).
34. Nemšák, S. *et al.* Concentration and chemical-state profiles at heterogeneous interfaces with sub-nm accuracy from standing-wave ambient-pressure photoemission. *Nat. Commun.* **5**, 5441 (2014).
35. Karslıoğlu, O. *et al.* An Efficient Algorithm for Automatic Structure Optimization in X-ray Standing-Wave Experiments. 1–25 (2018).
36. Fabbri, E. *et al.* Dynamic surface self-reconstruction is the key of highly active perovskite nano-electrocatalysts for water splitting. *Nat. Mater.* **16**, 925–931 (2017).
37. Liu, J. *et al.* Dynamic Lattice Oxygen Participation on Perovskite LaNiO 3 during Oxygen Evolution Reaction. *J. Phys. Chem. C* **124**, 15386–15390 (2020).
38. Rida, K., Peña, M. A., Sastre, E. & Martinez-Arias, A. Effect of calcination temperature on structural properties and catalytic activity in oxidation reactions of LaNiO3 perovskite prepared by Pechini method. *J. Rare Earths* **30**, 210–216 (2012).
39. McBean, C. L. *et al.* Generalizable, Electroless, Template-Assisted Synthesis and Electrocatalytic Mechanistic Understanding of Perovskite LaNiO3 Nanorods as Viable, Supportless Oxygen Evolution Reaction Catalysts in Alkaline Media. *ACS Appl. Mater. Interfaces* **9**, 24634–24648 (2017).
40. Retuerto, M. *et al.* Structural effects of LaNiO3 as electrocatalyst for the oxygen reduction reaction. *Appl. Catal. B Environ.* **203**, 363–371 (2017).
41. Rossmeisl, J., Qu, Z.-W., Zhu, H., Kroes, G.-J. & Nørskov, J. K. Electrolysis of water on oxide surfaces. *J. Electroanal. Chem.* **607**, 83–89 (2007).
42. Mefford, J. T., Zhao, Z., Bajdich, M. & Chueh, W. C. Interpreting Tafel behavior of consecutive electrochemical reactions through combined thermodynamic and steady state microkinetic approaches. *Energy Environ. Sci.* **13**, 622–634 (2020).

43. Rong, X., Parolin, J. & Kolpak, A. M. A Fundamental Relationship between Reaction Mechanism and Stability in Metal Oxide Catalysts for Oxygen Evolution. *ACS Catal.* **6**, 1153–1158 (2016).
44. Lee, Y.-L., Gadre, M. J., Shao-Horn, Y. & Morgan, D. Ab initio GGA+U study of oxygen evolution and oxygen reduction electrocatalysis on the (001) surfaces of lanthanum transition metal perovskites LaBO3 (B = Cr, Mn, Fe, Co and Ni). *Phys. Chem. Chem. Phys.* **17**, 21643–21663 (2015).
45. Back, S. *et al.* Prediction of Stable and Active (Oxy-Hydro) Oxide Nanoislands on Noble-Metal Supports for Electrochemical Oxygen Reduction Reaction. *ACS Appl. Mater. Interfaces* **11**, 2006–2013 (2019).
46. Doyle, A. D., Bajdich, M. & Vojvodic, A. Theoretical Insights to Bulk Activity Towards Oxygen Evolution in Oxyhydroxides. *Catal. Letters* **147**, 1533–1539 (2017).
47. Plessow, P. N., Bajdich, M., Greene, J., Vojvodic, A. & Abild-Pedersen, F. Trends in the Thermodynamic Stability of Ultrathin Supported Oxide Films. *J. Phys. Chem. C* **120**, 10351–10360 (2016).
48. Walton, A. S. *et al.* Interface Controlled Oxidation States in Layered Cobalt Oxide Nanoislands on Gold. *ACS Nano* **9**, 2445–2453 (2015).
49. Fester, J. *et al.* Edge reactivity and water-assisted dissociation on cobalt oxide nanoislands. *Nat. Commun.* **8**, 14169 (2017).
50. Mathew, K. *et al.* MPInterfaces: A Materials Project based Python tool for high-throughput computational screening of interfacial systems. *Comput. Mater. Sci.* **122**, 183–190 (2016).

METHODS

Density Functional Theory and calculation of the OER overpotentials. First-principles calculations were carried out using GGA-DFT with Hubard-*U* correction,[51–54] implemented with the Vienna Ab-initio Simulation Package (VASP)[55,56] interfaced with the Atomic Simulation Environment (ASE).[57,58] Projector augmented-wave potentials were used to replace the inner cores of the atom by all-electron, frozen-core.[59] Perdew-Burke-Ernzerhof exchange-correlation functional (PBE) was used to describe the exchange and correlation effects.[60] The Hubbard-*U* parameter applied to the *d*-electrons of the Ni-atoms (U_{eff}=*U*-*J*= 2 eV) was optimized to match our experimental strained lattice constants of LNO (a=b= 3.905 Å, c= 3.846 Å, see also Supplementary Fig. 16) and reported valence band photoemission data and magnetic structure.[61] For free-standing NiO_2, we used a more conventional U_{eff}=*U*-*J*= 5.5 eV established in previous studies of NiO_xH_y.[62] The convergence condition of the electronic SC-loop was set to be 10^{-5} eV. The LNO (001) slabs with Ni termination (LNO-Ni) and with La termination (LNO-La) were constructed with the fully relaxed LNO tetragonal bulk. The slabs were separated by an 18 Å vacuum gap and the bottom 4 layers of the 8-layer LNO-Ni and 9-layer LNO-La were fixed to simulate the LNO bulk. The slabs were optimized using a 4×4×1 Monkhorst-Pack grid[63] considering ferromagnetic ordering with cut-off energy of 500 eV. Dipole correction was applied to reduce the interactions between the periodically repeated slabs.

Next, the theoretical overpotentials for each surface were calculated using the standard OER mechanism which has been applied to many types of oxides[13,64–67] ($* \rightarrow$ OH*, OH* $\rightarrow$ O*, O* $\rightarrow$ OOH*, OOH* $\rightarrow O_2$(g)). The Gibbs free energies of each step of OER was calculated via the computational hydrogen electrode method[67] and includes a room temperature corrections, zero point energy (ZPE), and the vibrational enthalpy and entropy contributions (relative to H_2(*g*) and H_2O(*l*)) obtained by means of the harmonic approximation. The combined effect of free energy corrections and list of all total energies of adsorption is summarized in Supplementary Tables 3-5.

These tables also lists all reference structures and their respective energies with optimized structures

Thin film preparation. Thin films were grown by pulsed-laser epitaxy using the PLD/MBE2300 setup (PVD Products, USA, at Stanford University) or the Laser MBE (Surface GmbH, Germany, at Forschungszentrum Jülich GmbH) using target-to-substrate distances of 83 mm and 48 mm, respectively. The growth temperature was varied between front side temperatures of 450 and 750 °C as specified in the main text. The laser fluence was 1.6 J/cm^2 unless specified differently. The oxygen pressure during deposition was 15 mTorr. After each deposition, the samples were post-annealed at deposition temperature for 10 min in an atmosphere of 200 mTorr of oxygen and cooled down to temperatures below 300 °C within 5 minutes. All substrates were 10×10 mm^2 (001) Nb-doped $SrTiO_3$ (0.5 wt.% doping) or undoped $SrTiO_3$ (Shinkosha Co., Japan). Prior to the growth, the substrates were first etched in buffered HF (pH = 4.5) and then annealed at 950 °C for 2 h. The commercial 99.95 % elemental purity multiphase $LaNiO_3$ target (La_2NiO_4+NiO inclusions) was supplied by Toshima Manufacturing Co., Japan. Comparison to an in-lab sintered target fabricated with high purity (5N) metal oxide precursors showed no differences in growth parameters or electrocatalytic activity. The 99.99 % elemental purity NiO target was purchased from SurfaceNet GmbH, Germany. The growth was monitored *in situ* using a RHEED system (TorrRHEED^{TM}, Staib Instruments and kSA400, k-space Associates, Inc, respectively) operated at 35 kV (1.5 μA). Multilayers for SWXPS were deposited at 550 °C, with the commercial $LaNiO_3$ target and a $SrTiO_3$ single crystalline target (CrysTec GmbH, Germany).

Thin film characterization. X-ray diffractograms and reciprocal space maps were collected using PANalytical X'Pert PRO diffractometer equipped with a double monochromator and operating in a parallel-beam geometry. Atomic force microscopy was carried out without air exposure using an UHV Omicron VT-SPM XA operated in contact mode with tips coated with boron-doped polycrystalline diamond. The cantilever tips had a nominal radius of less than 150 nm and a spring constant of 25 N m^{-1} (AppNano, DD-ACTA-10). The force setpoint was limited to 2 nN in order to minimize a possible effect of the contact mode measurements on the surface morphology. XPS characterization without air exposure was performed with a PHI Versa Probe (Physical Electronics Inc., USA) with Al Kα X-ray illumination, a pass energy of 23.5 eV and at various photoemission angles without neutralization. The mean escape depth d is defined through the inelastic mean free path of photoelectrons $\lambda = 2.2$ nm (calculated via QUASES-IMFP-TPP2M)[69] and the photoemission angle θ through $d = \lambda \times \cos\theta$.[70] This isotropic approach uses the straight-line approximation,[71] as is suitable in the absence of well-characterized, material-specific angle-dependent effective attenuation lengths. For a full description of the information depth in photoemission, the readers are referred to refs. [70–72]. To calculate the surface stoichiometry from the measured intensities, we used the relative sensitivity factors provided by the instrument manufacturer and corrected these values to yield a La/Ni ratio of 1 for a stoichiometric, single phase, and freshly polished $LaNiO_3$ ceramic reference. The stoichiometry was determined based on the integrated raw peak areas after subtraction of a Shirley background. Fitting was performed using CasaXPS or KolXPD using the peak models described in Supplementary Note 4. For ICP-MS, the thin films were dissolved in 2 ml 10 % nitric acid and diluted with Milli-Q water to a total volume of 10 ml. The La/Ni ratio was determined using an Agilent 7900 ICP-MS in He collision cell mode (Agilent Technologies, Japan). PEEM experiments were carried out with the FE-LEEM P90 AC instrument commercialized by SPECS and installed as a permanent end-station at the soft X-ray undulator beamline UE56/1-SGM at the synchrotron facility BESSY II, Helmholtz-Zentrum Berlin. The LEED images were taken with an OCI BDL800IR-MCP LEED system using a beam voltage of 120 eV, a filament current of 2.78 A, a Wehnelt voltage of 2 V, a grid voltage of 100 V and a screen voltage of 3 kV.

Scanning transmission electron microscopy. Lamellar specimen for scanning transmission electron microscopy were prepared using focused ion beam milling with Ga in an FEI Helios NanoLab 600i or an FEI Helios NanoLab 460F1 dual-beam system.[73] Atomic-resolution high-angle annular dark-field (HAADF) STEM images and corresponding elemental maps were recorded at 200 kV in an FEI Titan G^2 80-200 ChemiSTEM microscope equipped with a high brightness FEG (XFEG), a probe spherical aberration corrector and a super-X EDXS system.[74] The incident electron beam convergence semi-angle for HAADF STEM imaging was ~25 mrad, while the collection semi-angle was 70-200 mrad.

Standing wave photoemission experiments. The measurements were carried out at the LBNL Advanced Light Source, using the ambient-pressure photoemission system at the Molecular Environmental Science beamline 11.0.2.[75] The SWXPS measurements were performed using a photon energy of 815 eV at an oxygen background pressure of 15 mtorr O_2. The samples were transferred from the deposition tool without exposure to atmosphere using glove bags filled with nitrogen. They were mounted using carbon tape and contacted with stainless steel clips in an Argon-filled glove box and transferred to the analysis chamber using the air-free transfer tool supplied by Sandia National Laboratories.

Electrochemical characterization. To perform electrochemical experiments with epitaxial thin films on 10×10×0.5 mm^3 single crystal substrates, we used a custom-made adapter to press the sample back side to the Pt plug of a rotating disk electrode (RDE, Pine Research). 50 nm Pt connections from the sample back side to the front side ensured ohmic contact to the LNO layer (Extended Data Fig. 5). On the front side, a film area of 0.75 mm diameter was exposed to the electrolyte and sealed using an O-ring (FFKM, Marco Rubber, USA). The RDE shaft was rotating at 1600 rpm. Electrochemical testing was performed using BioLogic VSP-300 or VSP-150 potentiostats, in a 150-mL alkaline-resistant Teflon cell (Pine Research) with a Pt wire as a counter electrode. Electrochemical impedance spectroscopy (EIS) was conducted with the amplitude of 20 mV at open circuit potential and the correction for the cell resistance (IR correction, typically 50-60 Ω) was based on the high-frequency intercept of the real impedance. The electrolyte solution of 0.1 M KOH, prepared by dissolving KOH pellets (Sigma-Aldrich, 99.99%) in deionized water (Millipore, >18.2 MΩcm), was O_2-saturated prior to testing for at least 30 minutes and maintained under O_2 atmosphere during testing. All electrochemical measurements were performed at room temperature. While higher electrolyte concentrations and temperatures can be used to test stability in application-near conditions,[5] 0.1 M KOH and room temperature represent the recommended best practices for comparison and benchmarking of model electrocatalyst systems.[76] Potentials were referenced to a Hg/HgO reference electrode (CHI Instruments, USA), which was periodically calibrated to the reversible hydrogen electrode (HydroFlex, USA) in 0.1 M KOH with typical values of ~880 mV. All OER testing was performed on a fresh electrode that had not undergone previous testing. Cyclic voltammetry was first performed in the pseudocapacitive redox phase change region (~0.9 to 1.6 V vs. RHE) at scan rates between 10 and 500 mV s^{-1}, followed by OER testing performed from 0.9 to 1.9 V vs. Hg/HgO at a scan rate of 10 mV s^{-1}. In the presented Tafel-like plots, data was capacitance corrected through averaging the forward and backward scans. The second cycle is shown for each sample. After electrochemical characterization, the samples were checked by XPS to verify the absence of Fe-contamination in the electrode surface.

UV-Vis spectroelectrochemistry experiments. For these experiments in transmission mode, LNO thin films on undoped, transparent, and double-side polished $SrTiO_3$ single crystal substrates were used. We performed the measurements in a custom-made spectroelectrochemical flow cell made from PEEK (IR correction ~350 Ω). The electrolyte flow was 0.1 mL min^{-1}. The potentials were referenced to a leakless miniature Ag/AgCl reference electrode (eDAQ, USA), which was periodically calibrated to the reversible hydrogen electrode in 0.1 M KOH with typical values of ~1050 mV. Cyclic voltammetry was performed between OCV and 1.55 V vs. RHE at various scan

rates of 10 mV s^{-1}, 1 mV s^{-1}, and 0.1 mV s^{-1} on all samples. Then, chronoamperometry was performed with potential holds up to 1.55 V, with 0.05 V intervals; each potential hold lasted for at least 40 min. At the end of each potential hold, spectra were collected with a deuterium tungsten-halogen light source (DH-2000-CAL, Ocean Optics, USA) and a UV-Vis spectrometer (USB-2000+, Ocean Optics, USA). Each spectrum was averaged over at least 5 sec of data acquisition. A reference spectrum was taken on an undoped $SrTiO_3$ single crystal in contact with the electrolyte.

DATA AVAILABILITY

The DFT data is available at https://www.catalysis-hub.org/publications/BaeumerTuning2020.[68] The experimental data is available via https://doi.org/10.26165/Juelich-Data/BMNAGT

METHODS REFERENCES

51. Anisimov, V. I., Zaanen, J. & Andersen, O. K. Band theory and Mott insulators: Hubbard U instead of Stoner I. *Phys. Rev. B* **44**, 943–954 (1991).
52. Anisimov, V. I., Solovyev, I. V., Korotin, M. A., Czyżyk, M. T. & Sawatzky, G. A. Density-functional theory and NiO photoemission spectra. *Phys. Rev. B* **48**, 16929–16934 (1993).
53. Solovyev, I. V., Dederichs, P. H. & Anisimov, V. I. Corrected atomic limit in the local-density approximation and the electronic structure of d impurities in Rb. *Phys. Rev. B* **50**, 16861–16871 (1994).
54. Anisimov, V. I., Aryasetiawan, F. & Lichtenstein, A. I. First-principles calculations of the electronic structure and spectra of strongly correlated systems: the LDA + U method. *J. Phys. Condens. Matter* **9**, 767–808 (1997).
55. Kresse, G. & Furthmüller, J. Efficient iterative schemes for ab initio total-energy calculations using a plane-wave basis set. *Phys. Rev. B* **54**, 11169–11186 (1996).
56. Kresse, G. & Hafner, J. Ab initio molecular dynamics for liquid metals. *Phys. Rev. B* **47**, 558–561 (1993).
57. Giannozzi, P. *et al.* QUANTUM ESPRESSO: a modular and open-source software project for quantum simulations of materials. *J. Phys. Condens. Matter* **21**, 395502 (2009).
58. Bahn, S. R. & Jacobsen, K. W. An object-oriented scripting interface to a legacy electronic structure code. *Comput. Sci. Eng.* **4**, 56–66 (2002).
59. Kresse, G. & Joubert, D. From ultrasoft pseudopotentials to the projector augmented-wave method. *Phys. Rev. B* **59**, 1758–1775 (1999).
60. Perdew, J. P., Burke, K. & Ernzerhof, M. Generalized Gradient Approximation Made Simple. *Phys. Rev. Lett.* **77**, 3865–3868 (1996).
61. Horiba, K. *et al.* Electronic structure of LaNiO3: An in situ soft x-ray photoemission and absorption study. *Phys. Rev. B* **76**, 155104 (2007).
62. Tkalych, A. J., Yu, K. & Carter, E. A. Structural and Electronic Features of β-Ni(OH)2 and β-NiOOH from First Principles. *J. Phys. Chem. C* **119**, 24315–24322 (2015).
63. Monkhorst, H. J. & Pack, J. D. Special points for Brillouin-zone integrations. *Phys. Rev. B* **13**, 5188–5192 (1976).
64. Bajdich, M., García-Mota, M., Vojvodic, A., Nørskov, J. K. & Bell, A. T. Theoretical Investigation of the Activity of Cobalt Oxides for the Electrochemical Oxidation of Water. *J. Am. Chem. Soc.* **135**, 13521–13530 (2013).
65. Friebel, D. *et al.* Identification of Highly Active Fe Sites in (Ni,Fe)OOH for Electrocatalytic Water Splitting. *J. Am. Chem. Soc.* **137**, 1305–1313 (2015).

66. Dionigi, F. & Strasser, P. NiFe-Based (Oxy)hydroxide Catalysts for Oxygen Evolution Reaction in Non-Acidic Electrolytes. *Adv. Energy Mater.* **6**, 1600621 (2016).
67. Nørskov, J. K. *et al.* Origin of the Overpotential for Oxygen Reduction at a Fuel-Cell Cathode. *J. Phys. Chem. B* **108**, 17886–17892 (2004).
68. Winther, K. T. *et al.* Catalysis-Hub.org, an open electronic structure database for surface reactions. *Sci. Data* **6**, 75 (2019).
69. Tanuma, S., Powell, C. J. & Penn, D. R. Calculations of electron inelastic mean free paths. V. Data for 14 organic compounds over the 50-2000 eV range. *Surf. Interface Anal.* **21**, 165–176 (1994).
70. Powell, C. J. Practical guide for inelastic mean free paths, effective attenuation lengths, mean escape depths, and information depths in x-ray photoelectron spectroscopy. *J. Vac. Sci. Technol. A* **38**, 023209 (2020).
71. Jablonski, A. & Powell, C. J. Practical expressions for the mean escape depth, the information depth, and the effective attenuation length in Auger-electron spectroscopy and x-ray photoelectron spectroscopy. *J. Vac. Sci. Technol. A Vacuum, Surfaces, Film.* **27**, 253–261 (2009).
72. Chambers, S. A. & Du, Y. Experimental determination of electron attenuation lengths in complex materials by means of epitaxial film growth: Advantages and challenges. *J. Vac. Sci. Technol. A* **38**, 043409 (2020).
73. Kruth, M., Meertens, D. & Tillmann, K. FEI Helios NanoLab 460F1 FIB-SEM. *J. large-scale Res. Facil. JLSRF* **2**, A59 (2016).
74. Kovács, A., Schierholz, R. & Tillmann, K. FEI Titan G2 80-200 CREWLEY. *J. large-scale Res. Facil. JLSRF* **2**, A43 (2016).
75. Frank Ogletree, D., Bluhm, H., Hebenstreit, E. D. & Salmeron, M. Photoelectron spectroscopy under ambient pressure and temperature conditions. *Nucl. Instruments Methods Phys. Res. Sect. A Accel. Spectrometers, Detect. Assoc. Equip.* **601**, 151–160 (2009).
76. Wei, C. *et al.* Recommended Practices and Benchmark Activity for Hydrogen and Oxygen Electrocatalysis in Water Splitting and Fuel Cells. *Adv. Mater.* **1806296**, 1806296 (2019).

ACKNOWLEDGMENT

This project was funded by the European Union's Horizon 2020 research and innovation programme under the Marie Sklodowska-Curie grant agreement No 796142. C.B., Q.L., J.T.M., A.Y.-L.L. and W.C.C. gratefully acknowledge financial support through the Department of Energy, Office of Basic Energy Sciences, Division of Materials Sciences and Engineering under contract no. DE-AC02-76SF00515. J.L. and M.B. acknowledge support by the U.S. Department of Energy, Office of Science, Office of Basic Energy Sciences, Chemical Sciences, Geosciences, and Biosciences Division, electrocatalysis Science Program to the SUNCAT Center for Interface Science and electrocatalysis. We also acknowledge funding from DFG (German Science Foundation) within the collaborative research center SFB 917. Part of this work was performed at the Stanford Nano Shared Facilities (SNSF)/Stanford Nanofabrication Facility (SNF), supported by the National Science Foundation under award ECCS-1542152. We thank HZB for the allocation of synchrotron radiation beamtime. This research used resources of the Advanced Light Source, a DOE Office of Science User Facility under contract no. DE-AC02-05CH11231. We thank Astrid Küppers (Forschungszentrum Jülich, ZEA-3) for the ICP-MS measurements and Prof. Florian Hausen and Dr. Silvia Karthäuser for helpful discussions and help in the LEED measurements. We thank Dr. Farid El Gabaly for supplying an air-free transfer vessel for SW-XPS analysis and Dr. Monika Blum for beamtime support. The authors would like to acknowledge the use of the computer time allocation for the m2997 allocation at the National Energy Research Scientific Computing Center, a DOE Office of Science User Facility supported by the Office of Science of the U.S. Department of Energy under Contract No. DE-AC02-05CH11231.

AUTHOR CONTRIBUTION STATEMENTS

C.B., Q.L., S.N., J.T.M, and W.C.C. conceived and designed the experiments. J.L. and M.B. designed, performed, analyzed, and interpreted the DFT simulations; C.B., Q.L., S.N., J.T.M., and W.C.C. contributed through in-depth discussion and comparison to the experiments during all stages. C.B., Q.L., A.Y.-L.L., and M.A.W. prepared the samples and performed thin-film and electrochemical characterization. C.B., S.G., and S.N. performed the standing-wave photoemission spectroscopy experiments. Q.L. modelled, analyzed and interpreted the standing-wave photoemission spectroscopy results; C.B., S.G., and S.N. contributed through discussion and interpretation. A.Y.-L.L. performed the UV-Vis spectroelectrochemistry analysis. H.P.M. performed the XPS cluster calculations. L.J. performed TEM analysis. T.D. performed the PEEM measurements and M.G. analyzed and quantified the PEEM data using PCA. M.G. and C.B. performed the LEED measurements. C.B., E.E.P., and J.T.M. analyzed the electrochemical performance of the thin films in the context of previous reports. R.D. and F.G. advised on the epitaxy approach to electrolysis and sample fabrication. C.B., J.L., Q.L., and M.B. wrote the manuscript with contributions from all authors. R.D., F.G., R.W., M.B., S.N., J.T.M., and W.C.C. supervised the research. C.B., R.W., M.B., S.N., J.T.M., and W.C.C. jointly determined the research direction.

COMPETING INTERESTS' STATEMENT

The authors declare no competing interests.

ADDITIONAL INFORMATION

Extended data is available for this paper at ...

Supplementary information is available for this paper at …

Correspondence and requests for materials should be addressed to C.B., M.B., and S.N.

Reprints and permissions information is available at www.nature.com/reprints.

EXTENDED DATA

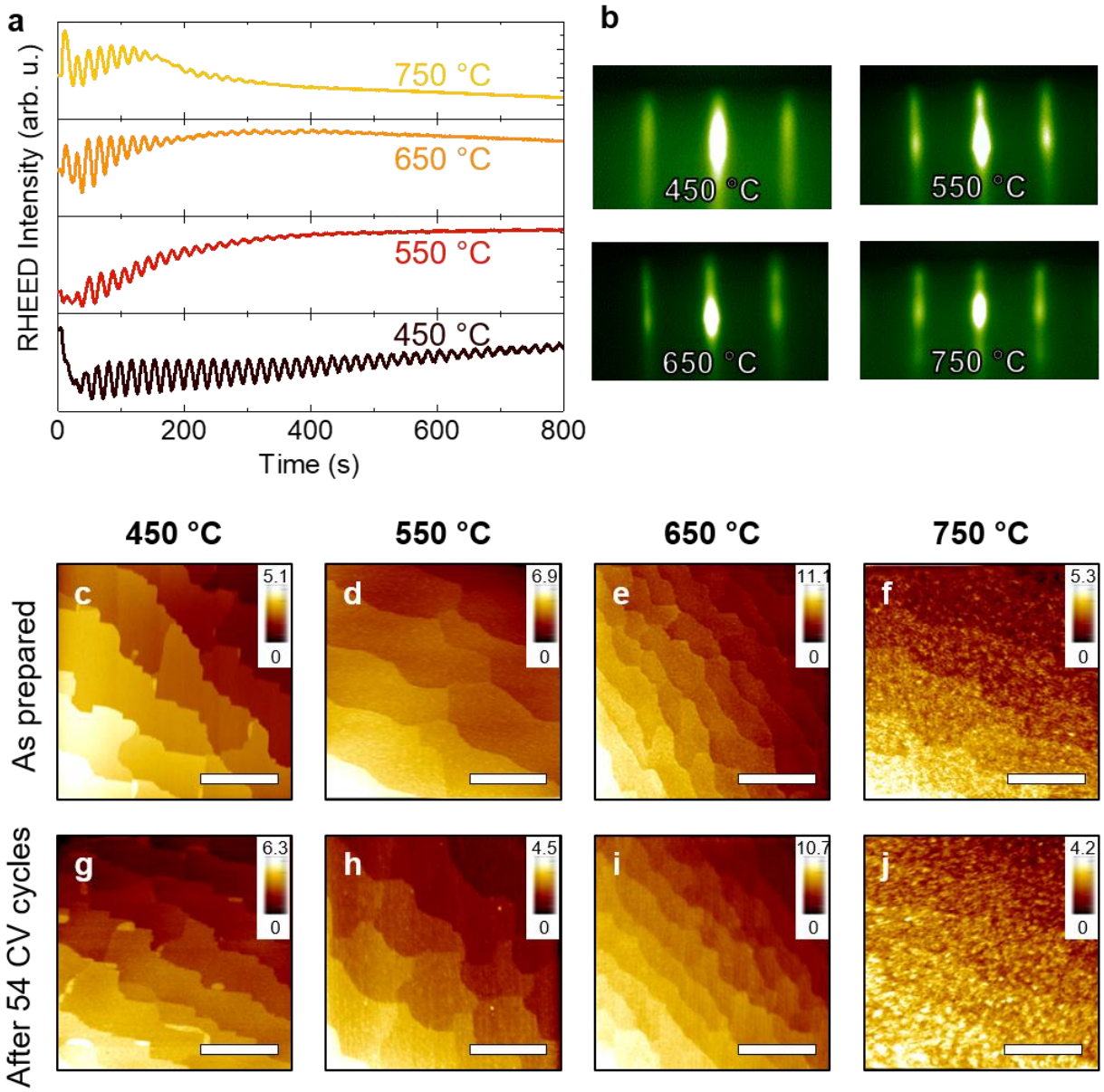

Extended Data Fig. 1: $LaNiO_3$ growth at different temperatures. a, RHEED intensity oscillations during growth at different T^{growth}. **b**, RHEED diffraction patterns after growth of 20 nm, confirming predominantly two-dimensional growth. **c-f,** AFM morphology in the as-prepared states for different T^{growth}. Scale bars are 1 µm, step height is ~0.4 nm. **g-j,** AFM morphology after cyclic voltammetry with 52 cycles with a maximum potential ~1.6 V vs. RHE and 2 cycles with maximum potential of ~1.9 V vs. RHE, revealing similar morphologies and similarly low roughness compared to the as-prepared state.

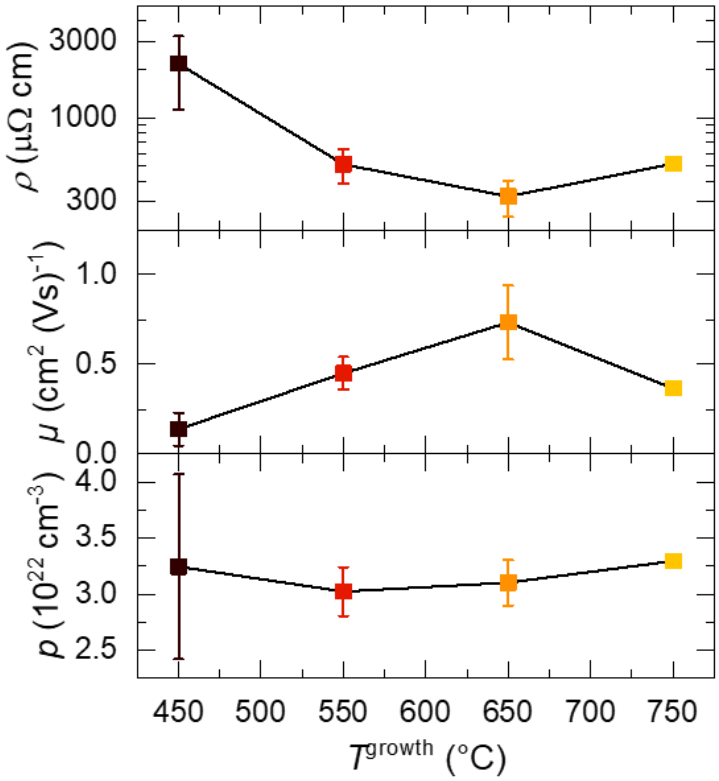

Extended Data Fig. 2: Electrical transport characterization. Hall resistivity (top), mobility (middle) and carrier concentration (bottom). Error bars indicate standard error from triplicate measurements.

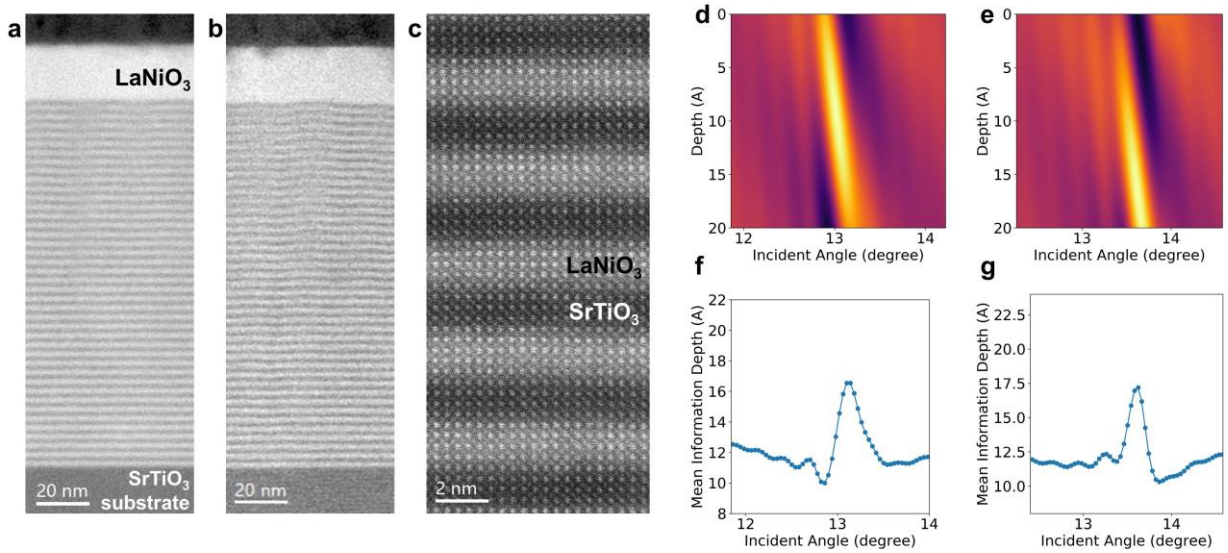

Extended Data Fig. 3: SW-XPS TEM images and variation of information depth. a, and **b,** Low-resolution high-angle annular dark-field HAADF STEM images of $LaNiO_3$ top layers deposited at 450 °C and 650 °C, respectively. The super lattice was deposited at 550°C in each case. **c,** High-resolution image of the super lattice revealing the four-unit-cell periodicity. **d,e,** The calculated standing-wave profile of electric field intensity ($|E^2|$) as a function of depth and incident angle for the standing wave samples with $LaNiO_3$ top layers deposited at 450 °C and 650 °C, respectively. **f,g,** Calculated mean information depth as a function of depth and incident angle based on the optimized structure for the standing wave samples with $LaNiO_3$ top layers deposited at 450 °C and 650 °C, respectively (Fig. 2b,c of the main text), derived through multiplication of electric field intensity ($|E^2|$) and photoelectron attenuation. Varying the incident angle changes the information depth deterministically. Simulating all XPS core level rocking curves simultaneously therefore allows to extract the compositional depth profile with atomic layer resolution.

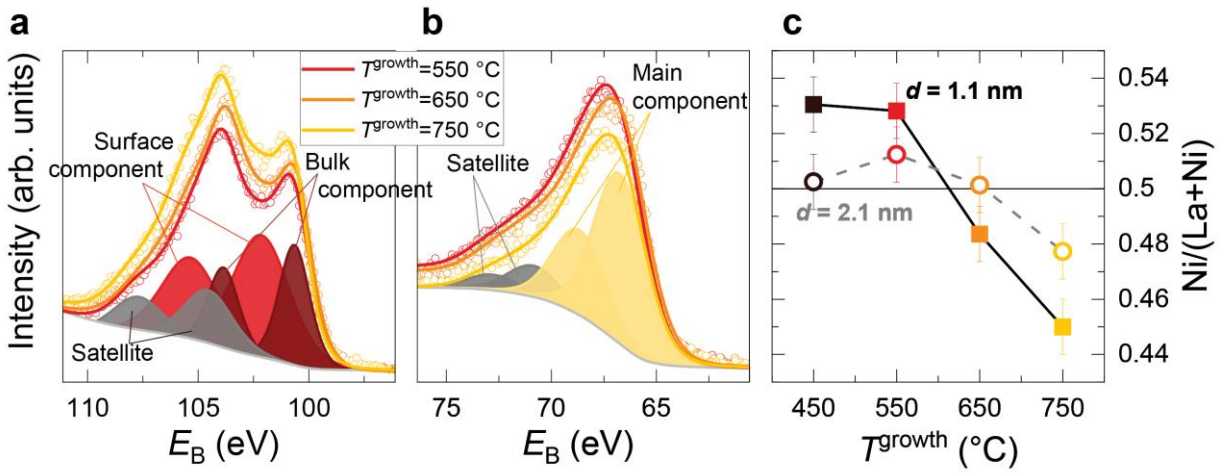

Extended Data Fig. 4: XPS surface composition a, La 4*d* laboratory XP spectra and **b,** Ni 3*p* spectra for different T^{growth}. Open circles show the data points, solid lines indicate the fitting result obtained (see Supplementary Note 4 for fitting details). Exemplary components used for the fit are shown for one spectrum each. **c,** Cation ratio as a function of T^{growth} for different mean escape depths *d*. Error bars indicate the maximum deviation from several measurements for a few identical samples measured under the same conditions.

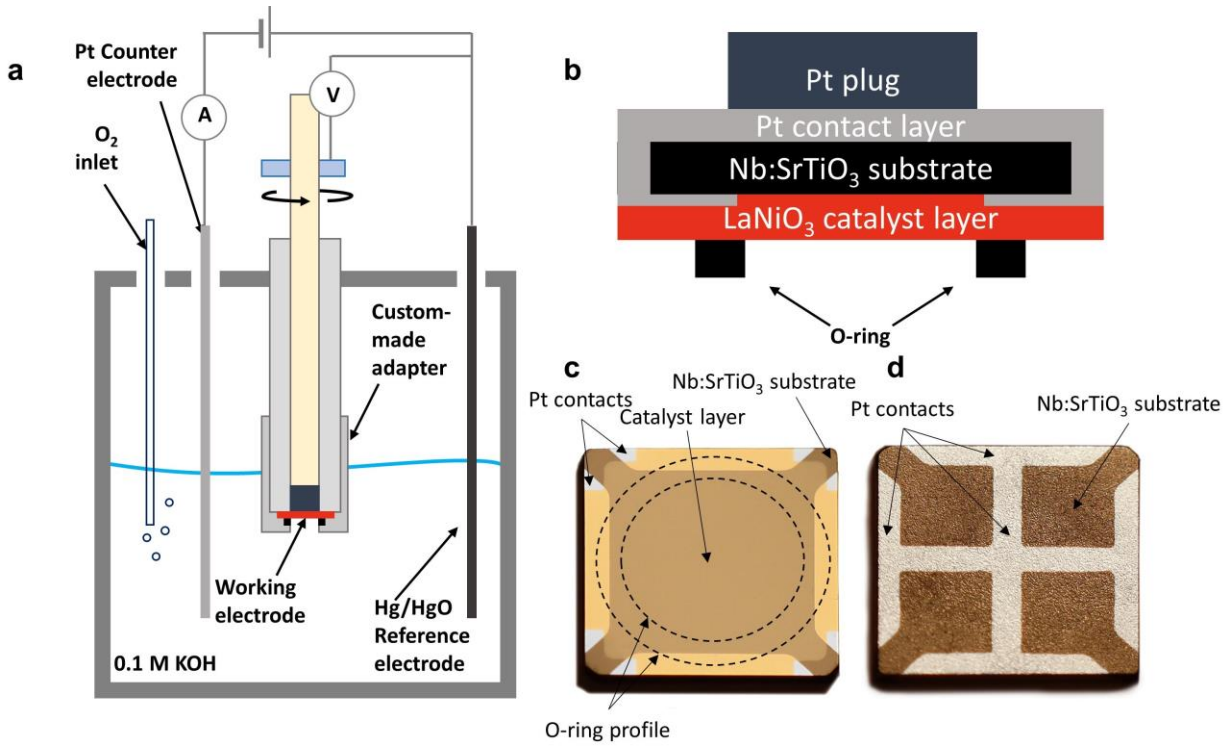

Extended Data Fig. 5: Rotating disc electrode setup for epitaxial thin films. a, Schematic of the rotating disc setup. **b,** Schematic of the sample contact. The Pt plug of the rotating shaft is connected to the sample back side. **c, d,** Optical images of the sample front and back side. A 50 nm Pt layer connects the sample back side to the substrate front side, forming ohmic electrical contact (R <10 Ω) with the back side of the $LaNiO_3$ catalyst layer. The electrode area is defined by a perfluoroelastomer (FFKM) O-ring fitted to the PEEK sample adapter. All experiments are performed without silver paste or epoxy adhesives. This leads to electrochemical investigation with a minimized amount of contaminating species.

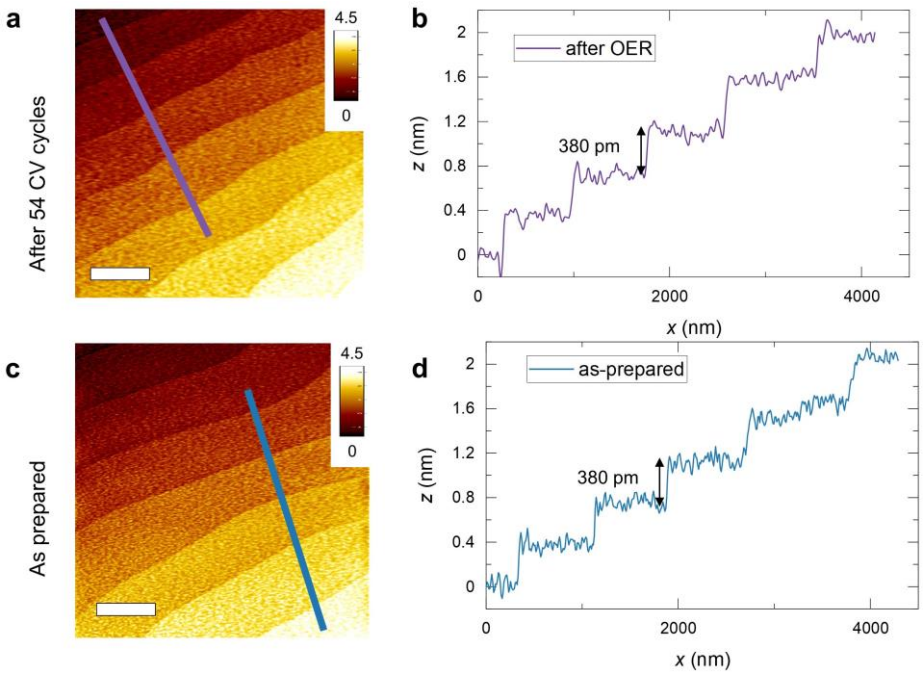

Extended Data Fig. 6: AFM investigation before and after OER. a, AFM morphology after 54 CV cycles **b,** Exemplary height profile extracted along the line in a, confirming unit cell height for all steps, indicating single termination. **c,** AFM morphology of the as-prepared state. **b,** Exemplary height profile extracted along the line in c, confirming unit cell height for all steps, indicating single termination.

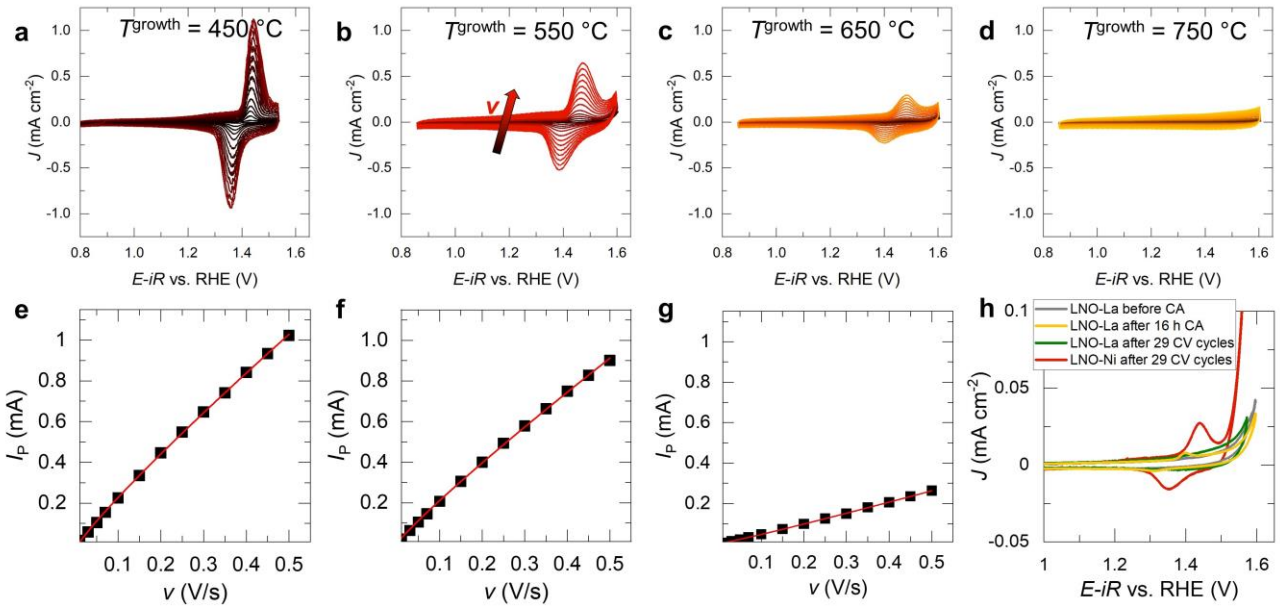

Extended Data Fig. 7: Sweep rate dependence of the redox peaks for samples with different growth temperature. **a-d,** Sweep rate-dependent cyclic voltammetry. **e-f,** Peak current as a function of sweep rate. Red lines indicate a power-law fit to the data with *b*-values of 0.90, 0.91, and 1.08 for panels a-c, respectively, indicating a surface-limited process. **h,** Redox behavior in cyclic voltammetry at 10 mV/s after various treatments. For LNO-La, the redox peak does not appear after 29 sweeps in cyclic voltammetry (green curve, 27 cycles with a maximum potential ~1.6 V vs. RHE and 2 cycles with maximum potential of ~1.9 V vs. RHE), nor after chronoamperometry (orange curve, potential stepped from 0.9 V up to 1.6 V in 50 mV steps and back down to 0.9 V in 100 mV steps; each step took 40 min, total time ~16 hrs). Similar results were obtained after a 38 h chronoamperometry at 1.63 V vs. RHE. For comparison, the redox peak for LNO-Ni after 20 sweeps in cyclic voltammetry is also shown (red curve).

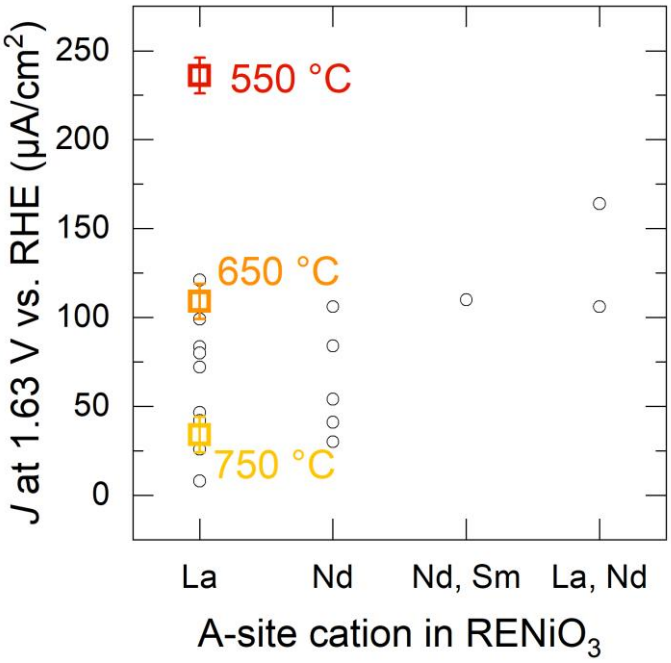

Extended Data Fig. 8: Comparison to literature. OER current density at 400 mV overpotential for different temperatures in comparison to activities previously reported for $RENiO_3$ epitaxial thin films. Literature references are listed in Supplementary Table 2.

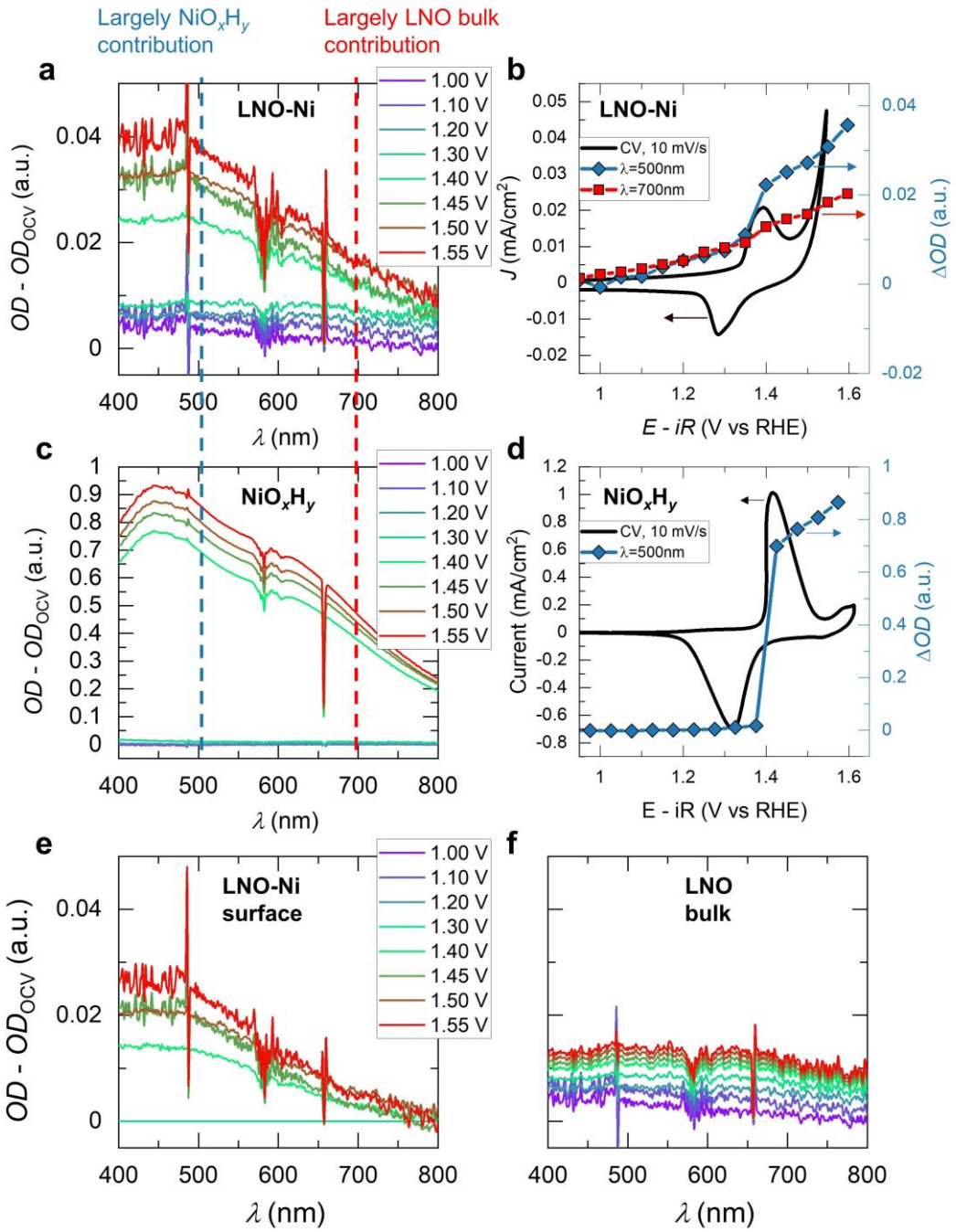

Extended Data Fig. 9: UV-Vis spectroelectrochemistry of $LaNiO_3$ and $Ni(OH)_2$. UV-Vis spectra of **a,** a 20 nm LNO-Ni film and **b,** a 50 nm electrodeposited $Ni(OH)_2$ film at various potentials, with optical density scaled relative to OCV (0.9 V vs. RHE). Note that the features around λ = 480 nm, 570-620 nm, and 660 nm are introduced during background subtraction as these are the emission lines from the deuterium light source. **c, d,** Changes in optical density at λ = 500 nm and 700 nm during potential holds plotted alongside the cyclic voltammetry results for $LaNiO_3$ and $Ni(OH)_2$, respectively. **e, f,** Spectral decomposition into surface and bulk spectra of a 20nm LNO film.

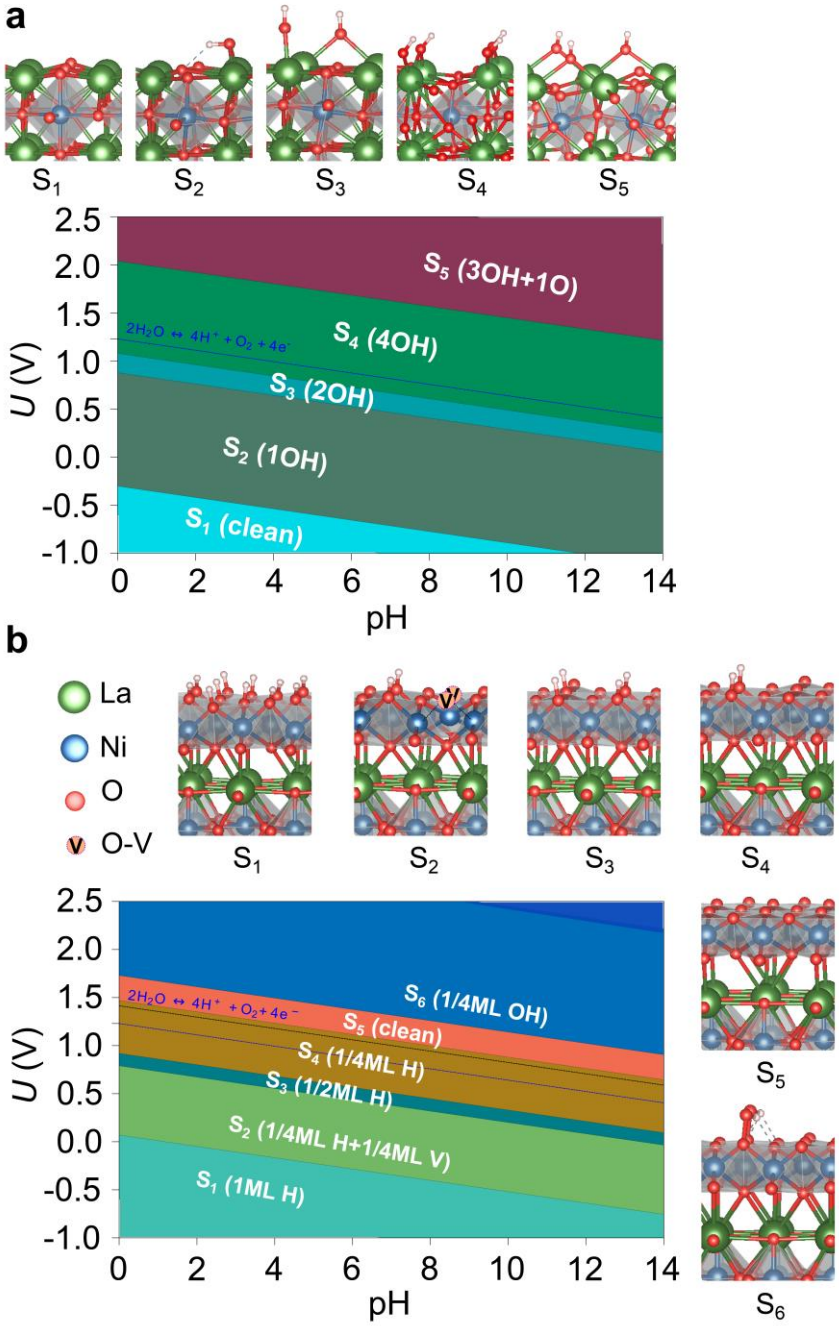

Extended Data Fig. 10: Surface Pourbaix diagram of LNO-La and NiO_2 | LNO-La.. a, Surface Pourbaix diagram of LNO-La with corresponding (2×2) structures as insets. Under OER conditions (U~1.68 V), LNO-La is fully covered with 4 OH* (1ML) at the La-O-La bridge sites. **b,** Surface Pourbaix diagram of LNO-La and NiO_2 | LNO-La with corresponding structures as insets. Under OER conditions (U~1.68 V), the clean (full ML of O_{3c}) surface (S_5) and ¼ monolayer (ML) OH covered surface followed by (S6) are the most favorable.

1